NASA Technical Memorandum 85986



# Unsteady Transonic Aerodynamic and Aeroelastic Calculations About Airfoils and Wings

Peter M. Goorjian and Guru P. Guruswamy

August 1984



NASA
National Aeronautics and
Space Administration

NASA Technical Memorandum 85986

# Unsteady Transonic Aerodynamic and Aeroelastic Calculations About Airfoils and Wings

Peter M Goorjian, Ames Research Center, Moffett Field, California
Guru P Guruswamy, Informatics General Corporation, Palo Alto, California

National Aeronautics and
Space Administration

**Ames Research Center**
Moffett Field California 94035

# UNSTEADY TRANSONIC AERODYNAMIC AND AEROELASTIC CALCULATIONS ABOUT AIRFOILS AND WINGS

Peter M Goorjian
NASA Ames Research Center
Moffett Field, California 94035, U S A

Guru P Guruswamy
Informatics General Corporation
Palo Alto California 94303, U S A

## SUMMARY

The development and application of transonic small-disturbance codes at NASA Ames Research Center for computing two-dimensional flows, using the code ATRAN2, and for computing three-dimensional flows, using the code ATRAN3S, are described Calculated and experimental results are compared for unsteady flows about airfoils and wings, including several of the cases from the AGARD Standard Aeroelastic Configurations In two dimensions, the results include AGARD priority cases for the NACA 64A006, NACA 64A010, NACA 0012, and MBB-A3 airfoils In three dimensions, the results include flows about the F-5 wing, a typical transport wing, and the AGARD rectangular wing Viscous corrections are included in some calculations, including those for the AGARD rectangular wing For several cases, the aerodynamic and aeroelastic calculations are compared with experimental results

## SYMBOLS

$b$ semichord of wing

$c$ full chord of wing

$C_{\ell_h}$ sectional lift coefficient due to plunging mode

$C_{\ell_\alpha}$ sectional lift coefficient due to pitching mode

$C_{m_h}$ sectional moment coefficient due to plunging mode

$C_{m_\alpha}$ sectional moment coefficient due to pitching mode

$k$ reduced frequency based on chord

$s$ semispan of the wing

$M, M_\infty$ free-stream Mach number

$U$ flutter speed

$x_\alpha$ sectional distance, measured in semichords, from the elastic axis to the mass center

$\mu$ wing-section-to-air-mass density ratio

$\phi$ disturbance velocity potential

$\omega_h$ bending natural frequency

$\omega_r$ reference frequency

$\omega_\alpha$ pitching natural frequency

## 1 INTRODUCTION

In the last decade, there have been extensive developments in computational, unsteady transonic aerodynamics (Refs 1 and 2) This growth in computational methods was in response to a need by engineers for computer codes with which to study fundamental aerodynamic and aeroelastic problems in the critical transonic regime For example, because the transonic flight regime provides the most efficient aircraft cruise performance (Refs 3 and 4), transonic flow fields constitute one of the most intensely studied problems in fluid dynamics Most large commercial aircraft cruise in the transonic regime However, the current total cost (Ref 5) of developing a modern transport aircraft is so large that it puts most of the resources, as well as the future reputation, of a company at risk Computational fluid dynamics (CFD) provides a new tool that in combination with the use of test facilities such as wind tunnels, provides aerodynamic design information with which to reduce this risk at the earliest possible phase of aircraft development

One of the major tasks in developing a new transport that involves unsteady transonic flow is the flutter analysis of the supercritical wings Experiments have shown (Ref 6) that dips in the flutter boundaries for wings occur at transonic Mach numbers and that such dips are especially severe for supercritical wings This occurrence of instabilities at lower dynamic pressures in the transonic regime is attributable to the motion of the shock waves that are present on the wings (Ref 7) Proper modeling of the physics of such moving shock waves requires that the CFD methods solve nonlinear partial differential equations for regions of mixed subsonic and supersonic flow At the present time, the most advanced codes use the small-disturbance, transonic potential equation, these codes are being used for generic research in aeroelasticity Currently, codes are being developed that use the more exact full-potential equation In comparison, for steady flows, practical applications use full-potential codes, and there is extensive development of Euler codes

The successful development and application of the two-dimensional code LTRAN2 (Ref 8), which solves the unsteady, transonic, small-disturbance potential equation using a time-integration method, and the availability of faster computers with larger memories made possible the development and use of the three-dimensional code XTRAN3S (Ref 9) In this code, the alternating direction implicit (ADI), finite-difference scheme (Ref 8) in LTRAN2 was extended to three-dimensional flow over wings In this conservative method, shock waves move in a time-accurate manner The XTRAN3S code can also perform static and dynamic aeroelastic computations by simultaneously integrating the aerodynamic and structural equations of motion This code is being used for both aerodynamic and aeroelastic applications (Refs 10-13)

Several efforts are in progress to develop two-dimensional and three-dimensional codes based on a full-potential theory (Refs 14-20) The reason for going to the more exact full-potential formulation from the approximating, small-disturbance one is to remove the accuracy limitations in the latter The removal of these limitations may be necessary to adequately model the flow over supercritical wings, and also to handle large perturbations in the flow However, by using the full-potential formulation, the major advantage of simplicity (imposing boundary conditions inherent in the small-disturbance theory) is lost Modeling a complex geometry (such as a wing, body, and nacelle) is fairly easy in small-disturbance theory, for the full-potential theory, however, the resultant computational meshes are quite complex This feature is one reason why full-potential codes are not as well developed as the small-disturbance potential codes

This report describes the development and application of transonic small-disturbance codes at NASA Ames Research Center for computing two-dimensional flows, using the code ATRAN2, and three-dimensional flows, using the code ATRAN3S Comparisons of calculated and experimental results are presented for unsteady flows about airfoils and wings, including several of the cases from the AGARD Standard Aeroelastic Configurations In two dimensions, the results include AGARD priority cases for the NACA 64A006, NACA 64A010, NACA 0012, and MBB-A3 airfoils In three dimensions, the results include flows about the F-5 wing, a typical transport wing, and the AGARD rectangular wing Viscous corrections will be included in some calculations, including those for the AGARD rectangular wing For several cases, the aerodynamic and aeroelastic calculations are compared with experimental results Brief descriptions are also given of recent improvements of the algorithms used in these codes, included are the addition of high-frequency terms and more accurate differencing in ATRAN2, and grid improvements in ATRAN3S for fighter-aircraft-type wings

## 2 ALGORITHM DEVELOPMENTS AND FLOW-FIELD CALCULATIONS TWO DIMENSIONS

In this section we shall describe algorithm and code improvements to the NASA Ames code LTRAN2 and then present comparisons of computed results and experimental data for the AGARD airfoils (Ref 21) The LTRAN2 code was introduced 7 years ago (Ref 8) Since then, its use has become routine (Refs 1 and 2) in generating unsteady, transonic air loads for oscillating airfoils, particularly for use in applications to aeroelasticity (Refs 22 and 23) During those 7 years, there have been many improvements in the accuracy, capability, stability, and efficiency of LTRAN2 Improvements in accuracy include the addition of high-frequency terms in the boundary conditions (Ref 24) and the governing equation (Ref 25), the inclusion of viscous effects (Refs 26-28), and the use of second-order-accurate spatial differencing (Ref 29) Wind-tunnel wall modeling (Ref 30) and supersonic free-stream (Ref 31) capabilities were added The stability of the code was improved by using monotone algorithms (Ref 32), and, finally, the efficiency of the code was improved by using nonreflecting far-field boundary conditions (Ref 33)

The improvement in stability with the monotone algorithm is shown in Fig 1 (Ref 32) The older method can become unstable at sonic expansion points and hence require a much smaller time-step for stable calculations (12 times smaller in this case)

The improvement in accuracy with second-order spatial differencing is shown in Figs 2 and 3 (Ref 29) for flow with type-B shock-wave motion Because of the large excursion in the shock wave, which the second-order method describes more accurately (Fig 2), the unsteady pressures (Fig 3) are more accurately described over a large portion of the airfoil by the second-order method

Figure 4 (Ref 25) shows the improvement in accuracy with the inclusion of high-frequency terms This modification did not require the addition of a third level of computer storage, as did previous methods, which can be an advantage especially when the method is extended to three-dimensional algorithms With the inclusion of these high-frequency terms in LTRAN2, the code is now valid at all frequencies This version of the NASA Ames code is designated ATRAN2 code

To account for viscous effects, two procedures are available in ATRAN2, a viscous-ramp method and a lag-entrainment method (Refs 27 and 28) For inviscid calculations, ATRAN2 solves the unsteady, transonic, small-disturbance potential equation (Refs 25 and 32)

$$k^2 M_\infty^4 \phi_{tt} + 2kM_\infty^2 \phi_{xt} = [(1 - M_\infty^2) - (\gamma + 1)M_\infty^m \phi_x]\phi_{xx} + \phi_{yy} \qquad (1)$$

The viscous corrections are implemented by modifying the inviscid airfoil tangency conditions, as well as the downstream wake conditions in the lag-entrainment method The viscous-ramp procedure is a phenomenological method in which a priori determined shape-changes simulating the viscous displacement effects are incorporated into the inviscid procedure Here the interaction between the shock and boundary layer is modeled by placing a wedge-nosed ramp at the base of the shock to obtain the reduced shock pressure rise The lag-entrainment equations are based on the boundary-layer assumption that the normal extent of the viscous region is small when compared with airfoil or wake thickness By integrating the governing partial differential equations in the normal direction and suitably modeling the requisite relationships, a set of three first-order ordinary differential equations, lag-entrainment equations," is obtained References 27, 28, 34, and 35 provide details on these methods and their use in ATRAN2

2 1 NACA 64A010 Airfoil

See Ref 34 for details on the procedures for generating the computed results Unsteady inviscid, wedge, and lag-entrainment solutions were obtained by forcing the airfoil to undergo sinusoidal motion and then integrating the flow equations in time, starting from the corresponding steady-state solutions A Fourier analysis of all three solutions was performed for pressure distributions for the third cycle of oscillation, and the real and imaginary parts of the first Fourier component were extracted These results were plotted after defining the pressure as

$$C_p = \text{(Re sin t - Im cos t)}$$

where is the amplitude of oscillation Unsteady aerodynamic coefficients were computed, based on the third cycle, for selected values of reduced frequencies Using these coefficients, flutter speeds were computed by the U-g method, following the procedure described in Ref 34 Two degrees of freedom, pitching and plunging, were assumed for the aeroelastic model

In Refs 36 and 37, steady and unsteady aerodynamic results for the NACA 64A010 airfoil, obtained in the Ames 11- by 11-Foot Transonic Wind Tunnel, are given for various flow conditions In this study, results are computed and compared with wind-tunnel results at a Reynolds number of 12 6 × $10^6$ for Mach 0 796 and a mean angle of attack of -0 21 The airfoil configuration is taken from the AGARD report (Ref 21)

Figure 5 shows the lower-surface, steady-pressure distributions obtained by computations and the experiment The viscous-ramp and the lag-entrainment methods compare better in predicting the shock location than does the inviscid method Unsteady aerodynamic results were obtained for the pitching motion of the airfoil at the five reduced frequencies – 0 05, 0 102, 0 202, 0 302, and 0 404 - that were considered in the experiment The inviscid and viscous-ramp calculations used 720 time-steps per cycle, the lag-entrainment method required 8000 In Fig 6, the plots of the magnitude and the corresponding phase angle of the lift coefficient versus the reduced frequency are shown, and Fig 7 shows the magnitude and phase angle of the moment coefficient about the leading edge as a function of the reduced frequency

For k = 0 101 and 0 404, Fourier analyses of all three solutions were performed for lower-surface pressure distributions for the third cycle of oscillation, and the real and imaginary parts of the first Fourier component were extracted A comparison of these results with experiment is shown in Figs 8 and 9 In general, the viscous solutions, particularly the lag-entrainment solution, are closer to the experimental results than is the inviscid solution

Using the U-g method, flutter speeds were computed based on the unsteady aerodynamic coefficients obtained by the computations and the experiment They were computed by assuming the elastic axis at the quarter chord, a = -0 5, the mass center at the midchord, $x_\alpha$ = 0 5, and the ratio of plunge-to-pitch natural frequencies $\omega_h/\omega_\alpha$ = 0 1 In Fig 10, the nondimensionalized flutter speed U, and the corresponding reduced frequency k, are shown versus the airfoil-to-air-mass density ratio, $\mu$ Flutter speeds obtained by the lag-entrainment solution are closer to those of the experiment than are the other two solutions In general, all three theoretical methods compare fairly well with the experiment in the reduced frequency, it is also observed that viscous effects have a tendency to reduce the flutter speed

Figure 11 is a time-history of the computed lower-surface pressures for the inviscid flow during the third cycle of motion Notice the motion of the shock wave and the change in shock strength To simulate the shock motion correctly, the governing equation was solved in conservative form Also notice the oscillations in pressures at the leading edge, which are due to the use of airfoil coordinates from the experimental model (Ref 36)

2 2 The MBB-A3 Airfoil

For this airfoil (Ref 34) results were computed and compared with those of experiment (Ref 38) at a Reynolds number of 6 × $10^6$ for a Mach number of 0 765 and a mean angle of attack of 1 5° (the design conditions for the airfoil) As was done in Ref 38, the Mach number and the angle of attack considered for computations were 0 7557 and 1 30°, respectively, thus matching the flow conditions in the wind tunnel The airfoil configuration is taken from the AGARD report (Ref 21)

Figure 12 shows the comparison of the steady-state pressure distributions for the upper and the lower surfaces The lag-entrainment solution compares well with the experiment The wedge solution is closer to the experiment than the inviscid solution Steady lifts obtained by inviscid, viscous ramp, lag-entrainment, and the experiment are 0 6667, 0 6433, 0 5377, and 0 5190, respectively

Unsteady aerodynamic results (Ref 34) were obtained by pitching the airfoil about the midchord with an amplitude of 1 0° for four reduced frequencies, 0 05, 0 10, 0 15, and 0 20 The unsteady inviscid, viscous-ramp, and lag-entrainment solutions were obtained starting from the corresponding steady-state solutions obtained earlier For all the cases considered, three cycles were required during which the transients disappeared and a periodic solution was obtained The inviscid and viscous-ramp calculations used 720 time-steps per cycle, and the lag-entrainment used 8000

For k = 0 1, a Fourier analysis of all three solutions was performed for the upper-surface pressure distributions for the third cycle of oscillation, and the real and imaginary parts of the first Fourier component were extracted A comparison of these results is shown in Fig 13 Using the U-g method, flutter speeds (Ref 34) were computed based on the unsteady aerodynamic coefficients obtained by the three methods The viscous methods increased the flutter speeds, but the reduced frequencies were essentially the same as those for the inviscid method

2 3 NACA 006 Airfoil

Three AGARD cases (cases 6, 8, and 10 in Ref 21) were computed for the NACA 006 airfoil and compared with experimental data (Ref 37) The computations were made using the experimental parameter given in Ref 37

For case 6, the values used were $M_\infty$ = 0 853, the dynamic flap amplitude $\delta_0$ = 1 1, k = 0 12, and the mean flap angle $\delta_m$ = 0 16 The number of time-steps per cycle was 720 for all the remaining two-dimensional results Only the inviscid and viscous-ramp methods were used for the remaining results because of the extremely small time-step size required for the lag-entrainment method

Figure 14 shows the comparison of pressures for the lower surface for steady flow, and Fig 15 shows the unsteady comparisons for the lower surface For all the remaining cases, the unsteady computational results were taken from the third cycle of motion Figure 16 shows a time-history of the lower-surface pressures for the inviscid results for the third cycle of flap motion Notice the motion of the shock wave and the change in its strength It essentially disappears during a portion of the cycle, that is, type B shock-wave motion This case demonstrates the need for a time-accurate formulation of the computed results Finally, notice the weak ridge and valley caused at the three-quarter chord location owing to the flap motion

For case 8 (Ref 21), $M_\infty$ = 0 877, k = 0 118, $\delta_0$ = 1 13, and $\delta_m$ = 0 15 Figure 17 shows the comparisons of steady pressures for the lower surface, and Fig 18 shows the unsteady flow comparisons The steady calculations predict too strong a shock wave, and this overprediction is carried over to the unsteady results, which show the effects of the shock motion As noted in Ref 37, these differences can be partially ascribed to wind-tunnel-wall interference In previous calculations (Ref 8) on this airfoil with an oscillating flap, similar differences were found between calculations and experiment, for the cases of type A, B, and C shock-wave motion For those cases, calculations that included wind-tunnel-wall simulations (Ref 30) also indicated that the differences might be due to wind-tunnel-wall interference

Figure 19 shows a time-history of the inviscid results Notice the motion of the shock wave and the changes at the flap hinge location Figure 20 shows the variation in the lift coefficient, $C_L$, during the third cycle of motion In comparison with harmonic approximations, zero through the first harmonic and zero through the fourth harmonic, Fig 20 shows that the variation is described by the first harmonic Figures 21 and 22 show the variations in lower shock position and strength during the third cycle, where the shock strength is taken to be the difference in pressure coefficients across the shock wave The shock-position variation is essentially simply harmonic, whereas the shock-strength variation contains higher harmonics This variation in shock position requires a method that allows the shock to move over the airfoil

For case 10 (Ref 21), $M_\infty$ = 0 879, k = 0 468, $\delta_0$ = 1 08, and $\delta_m$ = 0 01 Figure 23 shows the comparisons of steady pressures and Fig 24 shows the unsteady flow comparisons for the lower surface As in case 8, the calculations overpredict the shock strength in the steady flow, and the effects are carried over into the unsteady flow comparisons Notice the effects of increasing the frequency in comparing Figs 18 and 24 At the higher frequency, the shock motion is less and the real part of the pressure coefficients has a dip upstream of the shock wave Figure 25 shows a time-history of the inviscid results For this relatively high frequency, there is little shock-wave motion, as can be seen by comparing Figs 19 and 25

## 2 4 NACA 0012 Airfoil

For the NACA 0012 airfoil, most of the cases (Ref 21) required large mean angles of attack or large changes in the angle of attack that are typical for helicopter applications The only case that appears to be within the capability of the small-disturbance formulation is case 5 As we did for the previous airfoil, we have chosen to use the experimental parameters (Ref 37) for computing this case to compare with experimental data For case 5, $M_\infty$ = 0 755, k = 0 1628, the mean angle of attack $\alpha_m$ = 0 016°, and the dynamic pitch angle $\alpha_0$ = 2 51° The airfoil is pitching about the quarter-chord and that is where the moment coefficients are computed

Figure 26 shows the comparison of steady pressures for the upper surface Figure 27 shows comparisons at the eight times, during the cycle of motion, for which the experimental data (Ref 37) were given Figure 28 shows a time-history of the inviscid results For this high dynamic pitch angle, Fig 28 shows the creation, large motion, and disappearance of a strong shock wave Figures 29-33 show the variations, during the third cycle, of the lift coefficient $C_L$, of the quarter-chord moment coefficient $C_m$, of the drag coefficient $C_d$, of the upper shock position, and of the upper shock strength Figure 29 shows that $C_L$ is described adequately by the first harmonic Figure 30 shows that $C_m$ requires higher harmonics for an adequate description Figure 31 shows that $C_d$ is adequately described by the harmonics through the second, recall that for the drag, its fundamental harmonic is twice the first harmonic of the motion Figure 32 displays the shock-position variation and the portion of the cycle where the shock disappears Finally, Fig 33 shows the strong variation in shock strength, over the portion of the cycle where the shock disappears, there are no marks for actual shock strength

No results are shown for the NLR 7301 airfoil Calculations showed poor agreement with experiment Because of the thickness (16 5%) and leading-edge bluntness of this airfoil, it is probably outside the capability of the small-disturbance formulation

## 3 ALGORITHM DEVELOPMENTS AND FLOW-FIELD CALCULATIONS THREE DIMENSIONS

In this section, we shall describe the progress to date that has been made in a program at Ames Research Center for developing and applying an efficient computer code for calculating unsteady transonic flows in three dimensions We have chosen to develop further and to apply the XTRAN3S code, which was developed by Borland et al (Refs 39-41) under contract to the United States Air Force

The choice of XTRAN3S was based on several considerations First, XTRAN3S was a direct extension of LTRAN2 to three dimensions Hence, the successful results produced by LTRAN2 led us to expect that XTRAN3S would be an efficient and accurate tool for studying three-dimensional flows Like LTRAN2, the governing equation that is solved by XTRAN3S is the unsteady, transonic, small-disturbance equation in conservation form The use of the small-disturbance equation has the advantage of allowing the use of simple

computational grids for the unsteady flow about complex geometrical configurations, such as a wing, body, and canard, with, for example, moving control surfaces Since the algorithm relies on shock-capturing to account for the location and movement of shock waves, the equation is solved in conservative form, otherwise, erroneous shock locations and speeds will occur

The development of the Ames version of XTRAN3S, which is called ATRAN3S, proceeded as described below, where each of four developments is described in a separate subsection that also includes computational results The first effort was an aerodynamic and aeroelastic study (Refs 10 and 11) to compare XTRAN3S calculations with experimental data The purpose of that effort was to validate results obtainable from the code, as well as to determine the proper choice of numerical parameters, such as time-step size, in order to obtain accurate results In that first study, the simple case of a rectangular wing was examined

The next step (Ref 12) was to apply the code to a transport-type wing, characterized by a high-aspect ratio, large-taper ratio, and small sweep angle A flutter-analysis comparison was made with experimental data More recently (Refs 42 and 43), a study was made of the severe case of a fighter-type (F-5) wing, characterized by a low-aspect ratio, small-taper ratio, and large sweep angle Finally, a study (Ref 44) was made of the effects of viscosity and modes on the transonic aerodynamic and aeroelastic characteristics of wings The AGARD rectangular wing, as well as a typical transport wing, were examined The latter two studies required that algorithms be developed For the fighter wing, a new computational grid was developed in order to stabilize the calculations In the study of viscous effects, the manner of interacting the viscous and inviscid calculations was modified to eliminate numerical fluctuations in the pressure profiles at the shock locations

3 1 Aerodynamic and Aeroelastic Study Rectangular Wing

In this first study, XTRAN3S calculations for a rectangular wing were compared with experimental data The purpose was to validate XTRAN3S

Aerodynamic equations of motion- Many forms of the small-disturbance equations have been developed for computing the transonic flow field about wings (Refs 26 and 45) In this analysis, the modified unsteady, three-dimensional, transonic small-disturbance equation is used

$$A\phi_{tt} + B\phi_{xt} = (E\phi_x + F\phi_x^2 + G\phi_y^2)_x + (\phi_y + H\phi_x\phi_y)_y + (\phi_z)_z \qquad (2)$$

where $\phi$ is the disturbance velocity potential, $A = M_\infty^2$, $B = 2M_\infty^2$, $E = (1 - M_\infty^2)$, $F = -(1/2)(\gamma + 1)M_\infty^2$, $G = (1/2)(\gamma - 3)M_\infty^2$, and $H = -(\gamma - 1)M_\infty^2$

For the results shown in this section, the low-frequency form of this equation was solved by setting A to zero and using corresponding boundary conditions. The corresponding computer code, LTRAN3, was the earlier version of XTRAN3S and was the only version available at the time of this study (Ref 11) The code is based on a time-marching, finite-difference scheme following the first-order-accurate alternating direction implicit (ADI) algorithm A detailed description of the procedure is given in Ref 39 For details on the computational grid and the convergence criteria for the steady calculations, see Refs 10 and 11

Unsteady aerodynamic pressures were computed by forcing the wing to undergo a sinusoidal modal motion and integrating the aerodynamic equation of motion in time The modal motion assumed was the same as that simulated in the experiments For all the cases studied here, it was found that about three cycles of motion with 360 time-steps per cycle were sufficient to obtain a periodic aerodynamic response Periodicity was tested by comparing the responses of the second and third cycles The magnitudes and phase angles of the unsteady pressure jumps and corresponding force coefficients were computed using the third cycle

Aeroelastic equations of motion- Generalized coordinates (Refs 10 and 11) were used in deriving the aeroelastic equations of motion In this analysis, two generalized coordinates $h(t,y)$ and $\alpha(t,y)$, which correspond to bending displacement and torsional rotation of the elastic axis of the wing, respectively, were chosen as representative of the fluttering wing The generalized coordinates $h(t,y)$ and $\alpha(t,y)$ can be expressed as

$$h(y,t) = \bar{h}(t)f(y) , \qquad \alpha(y,t) = \bar{\alpha}(t)\theta(y)$$

where $\bar{h}(t)$ and $\bar{\alpha}(t)$ are unknown functions of time, and $f(y)$ and $\theta(y)$ are assumed semirigid modes For further details on the aeroelastic equations of motion, see Refs 10 and 11

The aeroelastic parameters and sign conventions for a typical section of the wing are shown in Fig 34 It is assumed that the wing is rigid in the chordwise direction, and that the amplitudes of oscillation are small It is also assumed that the principle of superposition of air loads is valid, even in the presence of shocks The validity of this assumption has been shown for two-dimensional cases both by experiment (Ref 36) and theory (Ref 23), provided the shock wave does not introduce separation and that the shock motion is small

Flutter solution procedure- A procedure based on the U-g method (Ref 46) was used to determine the transonic flutter boundaries Unsteady aerodynamic coefficients required in this work were the generalized lift and moment coefficients owing to modal motions corresponding to a pure bending mode $f(y)$ and a pure torsional mode $\theta(y)$ For the U-g method, unsteady aerodynamic coefficients, $\bar{C}_{\ell h}$, $\bar{C}_{\ell\alpha}$, $\bar{C}_{mh}$, and $\bar{C}_{m\alpha}$ are required as a function of reduced frequency for each mode In this analysis, the coefficients were computed at three reduced frequencies, and they were interpolated by a Lagrange interpolation scheme Since a low-frequency assumption was used in LTRAN3, the reduced frequencies considered were less than 0 4 (based on full chord)

Results Comparison of aerodynamic pressure coefficients- In Ref 47, experimental investigations were conducted on an unswept rectangular wing The wing had an aspect ratio of 3 with a 5%-thick biconvex

airfoil section Both steady and unsteady pressures were measured Unsteady pressures were measured while the wing was oscillating in its first bending mode

In Ref 11, steady and unsteady pressures from LTRAN3 were compared with the experimental data at Mach numbers of 0 7 and 0 9 for four span stations located at 0%, 50%, 70 , and 90% semispan For unsteady computations, the same bending mode that was measured in the experiment was also simulated in the code These results were also compared with corresponding data obtained in Ref 47 in which linear aerodynamic theory, based on the kernel function method, was used In the following results, the magnitude of the unsteady pressure jump is scaled by the induced angle of attack corresponding to the amplitude of the tip displacement, and the phase angle is defined as positive if the pressure leads the bending displacement The magnitude and phase angle from LTRAN3 correspond to the first fundamental harmonic in a Fourier series decomposition of the pressure time-history

In Fig 35, steady-pressure curves are compared between experiment and LTRAN3 at M = 0 9 at four spanwise stations The two sets of curves compare fairly well Except at the root section, pressure coefficients and shock locations obtained by LTRAN3 are in close agreement with those obtained from the experiment The discrepancies at the root section can be attributed mainly to the boundary layer on the wall, which was not considered in LTRAN3

In Fig 36, magnitudes $|\Delta C_p|$ and phase angles $\phi$ of the unsteady pressure jump obtained by LTRAN3, experiment, and kernel-function method are plotted at the 70% semispan station for M = 0 9 and $k_c$ = 0 26 In general, the two sets of curves obtained by LTRAN3 and experiment compare fairly well Peaks in pressure jumps occur at almost the same locations for both LTRAN3 and experiment As expected, linear theory results do not compare favorably, either with LTRAN3 or experiment, in the vicinity of shock

Results Comparison of flutter boundaries- Reference 48 reports an experimental investigation of the transonic flutter characteristics of unswept rectangular wings with aspect ratios of 5, and with circular-arc sections at various thickness ratios and Mach numbers See Refs 11 and 48 for details of the experimental models

In Refs 10 and 11 results obtained from LTRAN3 and from experiments were compared for four cases (1) 6% thick at M = 0 715, (2) 6% thick at M = 0 851, (3) 6% thick at M = 0 913, and (4) 4% thick at M = 0 904 These cases were selected so that Mach numbers ranging from a no-shock case to a strong-shock case were included Based on studies using LTRAN3, the Mach numbers considered in the experiment did not include a moderate-shock case for the 6%-thick model Thus, a case from the 4%-thick model was selected

Based on the unsteady aerodynamic coefficients obtained from LTRAN3, flutter boundaries were computed by the U-g method In Fig 37, results from LTRAN3 are plotted as a curve of flutter speed and corresponding reduced frequency versus wing-air-mass-density ratio for a 6%-thick model at M = 0 715 The corresponding curve obtained by the linear code NASTRAN is given in the same figure The experimental results available for a wing-air-mass-density ratio of 36 72 and a reduced frequency of 0 232 are also shown

Similar results were obtained for the other three cases Results for the four cases are given in Table 1 From this table it can be seen that the flutter speeds obtained by LTRAN3 are greater than those obtained by experiment On the other hand, the reduced frequencies obtained by LTRAN3 are lower than those obtained by the experiment, except for case 1 With the increase in Mach number, both LTRAN3 and the experiment show an increase in flutter speed, a decrease in reduced frequency, and an increase in density ratio Comparisons are better at lower Mach numbers Differences are quite significant at M = 0 904 and M = 0 913 These differences can be mainly attributed to the discrepancies between the aerodynamics of LTRAN3 and the experiment rather than to the flutter modeling

3 2 Flutter Analysis of a Transport Wing

The next step in evaluating the code XTRAN3S was to apply it to a flutter analysis of a transport-type wing (Ref 12) A search of the literature (Ref 12) available at that time revealed an appropriate set of experimental data with which to make comparisons in a Japanese report (Ref 49) The model configuration is shown in Fig 38 It has an aspect ratio of 8, a taper ratio of 0 4, a quarter-chord sweep of 20°, and a NACA 65A012 airfoil section See Ref 12 for a description of the model's structural and mass data

Steady and unsteady flows were calculated in the region of the transonic dip in the flutter boundary in the experimental data at Mach numbers of 0 75, 0 8, 0 825, and 0 85 Figure 39 shows the steady-flow pressure coefficients at M = 0 85 The flow is supersonic over a large portion of the wing and terminates in a shock at approximately the 65% chord line There were no aerodynamic data in Ref 49 with which to compare, although in Ref 12 comparisons were made with a standard code for steady flows and showed good agreement

Unsteady aerodynamic coefficients were calculated for the first three uncoupled vibration modes They were the first bending, second bending, and first torsion modes for a swept-wing beam model of the structure For each mode and Mach number, the wing was oscillated sinusoidally for three cycles at reduced frequencies that bracketed the expected flutter-reduced frequency Approximately 1200 time-steps per cycle were used for these calculations Figure 40 shows a comparison with linear theory for a reduced frequency k = 0 121 (near flutter) and a Mach number of 0 85 for the first bending mode There are substantial differences because of the transonic effects The larger leading-edge moment coefficients from XTRAN3S indicate a rearward shift of the aerodynamic center caused by the lift contribution of the shock-wave motion

Using these unsteady aerodynamic data, a flutter analysis was performed, using the U-g method (Ref 46) Figure 41 shows comparisons of flutter boundaries obtained from XTRAN3S, a doublet lattice analysis, and the experimental data The XTRAN3S results agree better with experiment than do the linear theory results Results for XTRAN3S are shown at Mach numbers of 0 75, 0 80, and 0 825 No flutter was predicted at Mach 0 85

3 3 F-5 Wing Analysis

Analysis- For nonrectangular wings, such as the F-5 wing, XTRAN3S used a sheared coordinate system, $\xi,\eta,\zeta$, in which the shearing occurs in the plane of the wing (Fig 42), where

$$\xi(x,y) = \frac{x - x_{LE}(y)}{x_{TE}(y) - x_{LE}(y)}, \qquad \eta(y) = y, \qquad \zeta(z) = z \tag{3}$$

After applying the transformation, Eq (2) is transformed to

$$\frac{\partial}{t}\left(-\frac{A\phi_t}{x} - B\phi\right) + \frac{\partial}{\partial}\left[\xi_x E)\phi_\xi + (\xi_x^2 F)\phi_\xi^2 + G(\xi_y\phi_\xi + \phi_\eta)^2 + \frac{\xi_y}{x}(\xi_y\phi_\xi + \phi_\eta) + H\xi_y\phi_\xi(\xi_y\phi_\xi + \phi_\eta\right]$$

$$+ \frac{\partial}{\partial\eta}\left[\frac{1}{\xi_x}(\xi_y\phi_\xi + \phi_\eta) + H\phi_\xi(\xi_y\phi_\xi + \phi_\eta\right] + \frac{\partial}{\partial\zeta}\left[\frac{\xi_\zeta}{\xi_x}\right] = 0 \tag{4}$$

The finite-difference computations are done in the $\xi,\eta,\zeta$ coordinate system, as indicated in Fig 42

This conventional shearing transformation, as given by Eq (3), is simple and adequate for wings with small sweep and large taper ratio (Refs 9-13) However, for wings with low aspect ratio, high sweep, and small taper ratio, such as fighter wings, use of this shearing transformation produces unstable calculations Since the transformation given by Eq (3) is only a function of the local chord, computational flow regions in the physical domain depend on the wing planform For delta-type wings, Eq (3) yields highly skewed flow regions and thus large discontinuous values for the metrics, $\xi_y$, near the upstream- and downstream-flow boundaries The metric $\xi_y$ appears as a coefficient of the cross derivatives in the governing equation, as given by Eq (4) Also, the far-field boundaries in the physical domain are not aligned with the flow directions These combined factors can make the flow computations unstable, as was the case for the F-5, AV-8B, and DAST ARW-2 wings (Ref 13)

The flow domain generated by Eq (3) will be illustrated for the F-5 wing Figure 43 shows the planform of the F-5 wing which has an aspect ratio of 2 98, a taper ratio of 0 31, and a leading-edge sweep angle of 31 92° The computational flow region that was obtained by using the shearing transformation, given by Eq (3), is shown in Fig 44 From this figure, the large skewness of the grid lines, which causes large gradients for the metrics near the flow boundaries, can be observed In fact, the scale in Fig 44 is stretched 10 to 1 in the y (or vertical) direction So the actual skewness is 10 times worse than shown Also the kinks (i e , discontinuities) in the upstream and downstream boundary grid lines are 10 times worse than shown It is at the downstream boundary at the location of the kink in the coordinate line (i e , at the wing tip span station) that numerical instabilities originate in the calculations for the F-5 wing

A modified shearing transformation was developed (Refs 42 and 43) that eliminated these numerical instabilities Like Eq (3), the modified transformation maps the physical wing into a rectangle, as indicated in Fig 42 Away from the wing, the modified transformation has the following characteristics (1) far-field boundaries are independent of the wing planform and aligned with respect to the free-stream direction, (2) smooth first and second derivatives occur for values of the metric quantities, particularly near boundaries, and (3) grid lines are clustered near the leading and trailing edges Figure 45 shows the computational flow region for the F-5 wing that was obtained by the modified shearing transformation Detailed comparisons of the metric quantity $\xi_y$ for the two methods are given in Ref 43 The new transformation, along with other improvements in XTRAN3S, has been incorporated into the Ames version of this code, which is called ATRAN3S

Results- In Ref 43, using the new transformation technique, steady and unsteady aerodynamic results were computed for the F-5 wing at M = 0 80, 0 90, and 0 95 and were compared with experimental measurements (Ref 50)

Figure 46 shows plots of steady pressure results obtained at M = 0 9 for the mid-semispan station by the two transformation methods and experiment In spite of using a time-step size of 0 001, results from the conventional shearing transformation eventually diverged Also, those results were highly inaccurate after 4000 time-steps, as illustrated in Fig 46 The computations diverged sometime after 4000 time-steps and before 6000 time-steps With the modified shearing transformation, a converged solution was obtained by using 2000 time-steps of size 0 01 In Fig 46, it can be seen that the latter method compares well with the experiment Plots of steady pressure distributions for four span stations obtained by the modified transformation and the experiment are given in Fig 47 Comparisons are generally good at all span stations

Figure 48 shows the modal motion used in the NLR experiment The wing is pitching about an axis located at the 50% root chord, and the pitching axis is normal to the wing root Figure 49 shows plots of the real and imaginary values of the upper-surface pressures at four span stations obtained by the modified shearing transformation and the NLR experiments at M = 0 9 These results were obtained for the wing oscillating at a frequency of 40 Hz

The same modal motion used in the NLR experiment was simulated in the code Results from the code were obtained by forcing the wing to undergo a sinusoidal modal motion for three cycles with 1200 time-steps per cycle, during which time the transients disappeared and a periodic response was obtained Because of the instabilities encountered during the steady calculations, no attempt was made to use the conventional shearing transformation

3 4 Effects of Viscosity and Modes

Analysis- In the final study (Ref 44), ATRAN3S was used to examine the effects of viscous corrections on the aerodynamics about wings and the effects of including higher structural modes in addition to the fundamental bending and torsion modes in transonic aeroelastic analyses Two wings were studied, a rectangular wing, with a NACA 64A010 airfoil section, and a swept wing, with an MBB-A3 supercritical airfoil section Viscous effects on both wings were analyzed by employing the viscous-wedge and lag-entrainment methods Aeroelastic analyses were performed and the effects of including the first two bending and torsion modes in the analysis were determined Results from this work show that the inclusion of viscous effects increases the flutter speed for the two wings studied For the rectangular wing, the fundamental modes were sufficient to determine the flutter speed, but the second torsion mode was required for an accurate aeroelastic analysis of the swept wing

Viscosity can play an important role in both the aerodynamic and aeroelastic characteristics of wings, as indicated in Ref 34, where the two-dimensional code, LTRAN2 (viscous) was used to study airfoils In transonic flow, viscous effects can alter the shock location and strength These changes in the pressure distribution along the chord will also influence the aeroelastic characteristics of the wing The ATRAN3S code was modified to include the effects of flow viscosity (Ref 41) Two models are used to account for the viscous effects in ATRAN3S The viscous wedge is an empirical method and the lag-entrainment method is based on a set of integral boundary-layer equations These methods are the same as those first incorporated into LTRAN2 (viscous) (Refs 28 and 41) The same viscous equations used in two dimensions are applied stripwise along the span to yield a three-dimensional correction

This viscous-wedge method is two dimensional and is applied to the wing at each spanwise coordinate Details of the computations can be found in Ref 44 A two-dimensional shock profile was used to determine the placement of the wedge in this study, as opposed to the three-dimensional shock profile discussed in Ref 41 This change was made to help reduce oscillations in the pressures obtained when using the viscous methods

Solutions obtained using the original viscous corrections contained high-frequency oscillations in the unsteady air loads An investigation into this problem determined that the shock sweep angles computed for the viscous-wedge corrections did not change smoothly across the span, but instead jittered in some span regions, as well as with time-step, at some span locations Also, it was determined that the use of these shock sweep angles to determine the shock location was not consistent with the method of locating the shock wave for use in the type-dependent differencing that is used in the inviscid calculations To correct this inconsistency, the shock location at each span station was determined by only using flow-field values along that span station This new method of determining the shock location was then used to place the viscous wedge on that span section As shown in Ref 44, large fluctuations in the pressure profile at the shock location were eliminated when the new method was used

For some calculations, the wedge model alone is sufficient for accurate determination of the unsteady viscous pressure distributions For other calculations, however, a more exact analysis is required to model the viscous effects To do this, the wedge correction is used along with a set of integral boundary-layer equations, the lag-entrainment equations, to perform viscous calculations downstream of the shock wave, including the downstream wake In this method it is assumed that viscous regions are small relative to the wing or wake thickness Details of the two methods are given in Refs 28, 34, and 41

In this study, the aeroelastic equations of motion for a cantilever wing were formulated using an assumed mode method (Refs 46 and 51) The superposition of the bending and torsion natural modes was used to describe the deflection shape of the wing at flutter It was assumed that the amplitude of oscillation was small, this was done so that the transonic aerodynamics from each mode of motion could be superposed (Ref 23) For details on the aeroelastic equations of motion, see Ref 44

A three-dimensional U-g type flutter analysis was used to obtain the flutter boundaries In this study, the first two bending and torsion modes were chosen to describe the motion of the low-aspect-ratio, rectangular, centilever wing Previous studies have shown that the fundamental modes are sufficient to determine the flutter speed of a rectangular wing in subsonic flow For comparison, the first two bending and torsion modes were also used for the swept wing

The generation of the aerodynamic data was performed separately from the aeroelastic analysis First, ATRAN3S was used to generate the steady and unsteady aerodynamic data by prescribing the wing motion These data were then input into the aeroelastic equations of motion to solve for the flutter speed The unsteady solutions were obtained by forcing the wing to oscillate sinusoidally as the aerodynamic equation of motion was integrated in time To obtain a steady solution, the amplitude of motion was set to zero The unsteady viscous calculations were restarted from corresponding steady-state solutions For unsteady calculations, three cycles of motion were sufficient for the transients to die out and for a periodic solution to be obtained For most inviscid calculations, 360 time-steps per cycle were used Viscous calculations typically required 720 time-steps per cycle for the wedge calculations and 2160 time-steps per cycle for the lag-entrainment calculations Unsteady aerodynamic coefficients, based on the third cycle, were used to compute flutter boundaries for inviscid and viscous calculations For the rectangular wing, unsteady calculations were made for four modes at four different Mach numbers and from three to six reduced frequencies for each Mach number Also the inviscid and the two viscous methods were considered Only limited results were computed for the swept wing

Results Rectangular wing with NACA 64A010 airfoil- One of the two wings considered in this study was the AGARD rectangular wing with an aspect ratio of 4 and a NACA 64A010 airfoil cross section Aerodynamic and flutter results were computed for the rectangular wing at $M = 0.8$ and at zero angle of attack, which is one of the AGARD suggested flow conditions (Ref 52) In addition, calculations for the same wing were made at $M = 0.70$, $M = 0.85$, and $M = 0.90$ to determine the effects of Mach number on three-dimensional aeroelastic calculations First, steady-state pressure distributions were obtained for the inviscid, wedge, and lag-entrainment methods The steady wedge calculations were restarted from the steady inviscid solution, and the steady lag-entrainment calculations were restarted from the steady wedge

solution Figure 50 shows the steady pressure profiles for the inviscid flow at M = 0 85 Figure 51 shows the steady pressure distribution for the three methods at the 60% semispan station and at three Mach numbers The code diverged when the lag-entrainment method was used at M = 0 90, so no results were obtained for those conditions The forward displacement of the shock and reduction in strength are characteristic of viscous flow These trends are consistent with those shown in two dimensions for the same airfoil It can be seen that the lag-entrainment method shows no deviation from the wedge for this particular wing

The first and second bending and first and second torsion natural modes were selected to accurately model the motion of the wing to obtain unsteady aerodynamic coefficients Calculations were made at reduced frequencies, based on full chord, from 0 1 to 0 6 The maximum deflections were 3 44° for the torsion modes and 10% of the chord for the bending modes The wing was constrained to pitch about the midchord Figure 52 shows the magnitude of the unsteady local lift coefficient and the corresponding phase angle versus span for the rectangular wing at three Mach numbers Results are shown for inviscid and for both the wedge and lag-entrainment viscous correction methods for the first torsion mode at a reduced frequency of 0 4 As expected from two-dimensional studies (Ref 34), the lift coefficients obtained by the viscous methods are lower than those calculated using the inviscid method, however, the magnitude of the lift using the wedge correction shows little change over the inviscid method The phase angles show a significant change for both viscous methods

As mentioned earlier, the flutter boundaries were determined using a three-dimensional U-g method Of primary interest in this study were the aeroelastic characteristics of the rectangular wing related to the effects of the structural modes and flow viscosity Four combinations of the first two pure bending and torsion modes were considered First, only the first bending and first torsion modes were included Then the second modes of each type were added individually Finally, all four modes, namely, first bending, second bending, first torsion, and second torsion, were all included in the solution For the modal analysis, the wing was configured so that the elastic axis and center of mass were located at 45% and 60% of the chord, respectively, aft of the leading edge All other aeroelastic parameters were set to represent a typical wing For the rectangular wing, the first bending and torsion modes were sufficient to determine the flutter speed (Ref 44) The flutter frequency in all cases is very close to the first bending frequency, which explains the dominance of the first bending mode Figure 53 shows the deflection of the wing at flutter It closely resembles the first bending mode Many of the aeroelastic parameters were varied to see if any effect of the higher modes could be obtained, little to no effect was seen Only when very unrealistic values were used was any significant effect of modes noticed At all Mach numbers, the first bending and torsion modes are all that are required for an aeroelastic analysis of a small-aspect-ratio, unswept, rectangular wing in subsonic or transonic flow

The effect of flow viscosity is an important factor to consider when computing the flutter boundaries of a wing in transonic flow Viscosity can have a noticeable effect on the aerodynamic forces acting on the wing and, hence, on the flutter boundaries Viscous calculations were made at three Mach numbers, M = 0 80, M = 0 85, and M = 0 90 For each Mach number, aerodynamic coefficients were calculated over a range of reduced frequencies from 0 1 to 0 6 and for the same four structural modes discussed earlier The wedge and lag-entrainment viscous methods were used At M = 0 85, the flow was transonic and the shock was well defined The lift coefficients calculated with viscous corrections included were slightly below the inviscid calculations This is the trend that was anticipated because it corresponds to trends shown for two-dimensional airfoils This small reduction in force, coupled with significant changes in the phase angles, contributes to the higher flutter speeds shown for the viscous methods in Fig 54 (Ref 44) A well-defined transonic dip can be seen in Fig 54, with the lowest flutter speed occurring between M = 0 85 and M = 0 90

Inclusion of the viscous corrections resulted in about a 10% increase in flutter speed The increase in flutter speed is a direct result of the viscous corrections causing a reduction in the magnitude of the lift coefficient A higher flutter speed does not always follow from a reduction in magnitude of the lift because the change in phase angle must also be considered when one is trying to anticipate flutter trends The wedge correction required little more computational effort than the inviscid method, but yielded an increase in flutter speed, as is depicted in Fig 54 The lag-entrainment method on the other hand, required 6 to 8 times the computing time to obtain a converged, stabilized solution The results obtained using the lag-entrainment method were about the same as the wedge correction provided It is noted that the wedge calculations were performed at 720 time-steps per cycle, and the lag-entrainment calculations were performed at 2160 time-steps per cycle Both of these are substantially less than were used in the earlier two-dimensional calculations reported in Ref 34

Results Swept wing with MBB-A3 airfoil- This swept wing with an MBB-A3 airfoil section was chosen to represent a typical transport-type wing It has a full-span aspect ratio of 8, a taper ratio of 0 4, a leading-edge sweep angle of 25°, and an MBB-A3 supercritical airfoil section Because of the complex geometry, the computing time required per case was twice that required for similar calculations on the rectangular wing Aerodynamic and flutter calculations were made inviscidly, as well as by using the wedge and lag-entrainment viscous corrections at a Mach number of M = 0 85 As was done for the rectangular wing, steady-state data were computed, and then the unsteady runs were restarted from the corresponding steady-state data files

The first bending, first torsion, second bending, and second torsion modes were incorporated into the flutter analysis of the swept wing (Fig 55) Again, the deflections of the wing were computed for each mode at 507 wing locations to describe the deflection shapes in the transonic code It can be seen that the modes, despite the sweep and taper, are very similar to the corresponding modes for a cantilever beam To obtain a converged inviscid solution, 720 time-steps per cycle were required, 1440 and 2880 time-steps per cycle were required for the viscous wedge and lag-entrainment methods, respectively Calculations were made at k = 0 4, 0 5, 0 6, and 0 7 for all three methods

Figure 56 shows the inviscid steady-pressure distribution across the swept wing for M = 0 85 The steady pressure across the chord, at the 60% semispan location, is shown in Fig 57 for all three methods and for both the upper and lower surfaces The viscous wedge shows a shock which has moved forward of the

inviscid shock and is much weaker The lag-entrainment correction causes the shock to move still farther forward For this wing and airfoil section, the lag-entrainment method does show a significant change from the viscous wedge method

Flutter calculations were performed on this wing at M = 0 85, the results are shown in Table 2 Here again, the primary modes dominate the flutter solution For this wing, however, the second torsion mode does cause a noticeable change in the flutter speed When the second bending mode was added to the primary modes, only an insignificant change in the flutter speed was noted, but when the second torsion mode was added, the flutter speed decreased by about 5% It was expected that the torsion modes would play an important role in this analysis because of the sweep of the wing The first two torsion modes can be seen along with the first bending mode in Fig 58

## 4 CONCLUDING REMARKS

Two computer codes, ATRAN2 and ATRAN3S, were used to compute unsteady transonic flows about airfoils and wings, and the results were compared with experimental data Both codes solve the unsteady, transonic small-disturbance equation in conservative form, and viscous corrections are made through the use of either the viscous wedge or lag-entrainment methods The ATRAN2 code computes two-dimensional flows about airfoils, and ATRAN3 computes three-dimensional flows about wings

The comparisons with experimental data showed good agreement, in general, and included several of the test cases from the AGARD Standard Aeroelastic Configurations For some cases, aeroelastic calculations were made, and the transonic dip in the flutter boundary was demonstrated For the transport-type wing, experimental flutter data were available, and the calculated results were in good agreement with them For some airfoil cases, including the NACA 0012 airfoil, during the airfoil motion there were large variations in the location and strength of the shock waves These cases demonstrated the need for codes to solve the governing equations in conservation form in order to accurately simulate the unsteady flow

Several improvements in the algorithms were described, including improvements for high-frequency accuracy, numerical stability, and second-order spatial differencing accuracy for ATRAN2, the grids for fighter-type wings and viscous-inviscid algorithm interactions for stability for ATRAN3S were also improved

These calculations demonstrate that ATRAN2 and ATRAN3S are ready for use by aerodynamicists and aeroelasticians in practical applications involving unsteady transonic flows for which the limitations of small-disturbance theory are valid

## REFERENCES


1 Goorjian, P M , "Computations of Unsteady Transonic Flows " In Recent Advances in Numerical Methods in Fluids Vol IV Advances in Computational Transonic, ed W G Habashi, Pineridge Press Ltd , U K , 1984

2 Ballhaus, W F , Deiwert, G S , Goorjian, P M , Holst, T L , and Kutler, P , "Advances and Opportunities in Transonic Flow Computations " In Numerical and Physical Aspects of Aerodynamic Flows, Springer, 1981

3 Ballhaus, W F , "Some Recent Progress in Transonic Flow Computations " Numerical Methods in Fluid Dynamics, Chap 3, eds H J Wirz and J J Smoldren, 1976

4 Holst, T L , "Numerical Computation of Transonic Flow Governed by the Full-Potential Equation " VKI Lecture Series Computational Fluid Dynamics, von Karman Institute for Fluid Dynamics, Rhode-St -Genese, Belgium, Mar 7-11, 1983

5 The Influence of Computational Fluid Dynamics on Experimental Aerospace Facilities, A Fifteen Year Projection National Research Council Report, National Academy of Sciences, National Academy Press, Washington, D C , 1983

6 Farmer, G M , and Hanson, W P , "Comparison of Supercritical and Conventional Wing Flutter Characteristics " Proceedings AIAA/ASME/SAE 17th Structures, Structural Dynamics and Materials Conference, King of Prussia, Pa , Apr 1976 (Also NASA TM X-72837, 1976 )

7 Ashley, H , "Role of Shocks in the Sub-Transonic Flutter Phenomenon " J Aircraft, Vol 17, Mar 1980, pp 187-197

8 Ballhaus, W F , and Goorjian, P M , "Implicit Finite-Difference Computations of Unsteady Transonic Flows about Airfoils " AIAA J , Vol 15, Dec 1977, pp 1728-1735

9 Borland, C J , and Rizzetta, D P , "Transonic Unsteady Aerodynamics for Aeroelastic Applications Vol I Technical Development Summary " AFFDL-TR-80-3107, Air Force Flight Dynamics Laboratory, Wright-Patterson AFB, Ohio, June 1982

10 Guruswamy, P , and Goorjian, P M , "Comparisons between Computations and Experimental Data in Unsteady Three-Dimensional Transonic Aerodynamics, Including Aeroelastic Applications " AIAA Paper 82-0690-CP, 1982

11 Guruswamy, P , and Goorjian, P M , "Computations and Aeroelastic Applications of Unsteady Transonic Aerodynamics about Wings " J Aircraft, Vol 21, No 1, Jan 1984, pp 37-43

12 Myers, M R , Guruswamy, P , and Goorjian, P M , "Flutter Analysis of a Transport Wing Using XTRAN3S " AIAA Paper 83-0922, 1983

13 Seidel, D A , Bennett, R M , and Ricketts, R H , "Some Recent Applications of XTRAN3S " NASA TM-85641, 1983

14 Goorjian, P M , "Implicit Computations of Unsteady Transonic Flow Governed by the Full Potential Equation in the Conservation Form " AIAA Paper 80-0150, 1980

15 Sankar, N L , Malone, J B , and Tassa, Y , "An Implicit Conservative Algorithm for Steady and Unsteady Three Dimensional Transonic Flows " AIAA Paper 81-1016, Palo Alto, Calif , 1981, pp 199-212

16 Malone, J B , and Sankar, N L , "Numerical Simulation of 2-D Unsteady Transonic Flows Using the Full-Potential Equation " AIAA Paper 83-0233, 1983

17 Malone, J B , and Sankar, N L , "Numerical Solutions of 2-D Unsteady Transonic Flows Using Coupled Potential-Flow/Boundary-Layer Methods " AIAA Paper 84-0268, Jan 1984

18 Malone, J B , and Sankar, N L , "Full-Potential Solutions for Transonic Flows about Airfoils with Oscillating Flaps " AIAA Paper 84-0298, 1984

19 Bridgeman, J O , Steger, J L , and Caradonna, F X , "A Conservative Finite Difference Algorithm for the Unsteady Transonic Potential Equation in Generalized Coordinates " AIAA Paper 82-1388, San Diego, Calif , 1982

20 Isogai, K , "Calculations of Unsteady Transonic Potential Flow over Oscillating Three-Dimensional Wings " NAL TR-706T, National Aerospace Laboratory, Tokyo, Japan, Mar 1982

21 Bland, S R , "AGARD Two-Dimensional Aeroelastic Configurations " AGARD AR-156, 1979

22 Ballhaus, W F , and Goorjian, P M , "Computation of Unsteady Transonic Flows by the Indicial Method " AIAA J , Vol 16, No 2, Feb 1978, pp 117-124

23 Guruswamy, P , and Yang, T Y , "Aeroelastic Time Response Analysis of Thin Airfoils by Transonic Code LTRAN2 " Computers and Fluids, Vol 9, No 4, Dec 1980, pp 409-425

24 Hessenius, K A , and Goorjian, P M , "Validation of LTRAN2-HI by Comparison with Unsteady Transonic Experiment " AIAA J , Vol 20, No 5, May 1982, pp 731-732

25 McCroskey, W J , and Goorjian, P M , "Interactions of Airfoils with Gusts and Concentrated Vortices in Unsteady Transonic Flow " AIAA Paper 83-1691, Danvers, Mass , 1983

26 Yoshihara, H , "Formulation of the Three-Dimensional Transonic Unsteady Aerodynamic Problem " AFFDL-TR-79-3030, Air Force Flight Dynamics Laboratory, Wright-Patterson AFB, Ohio, Feb 1979

27 Rizzetta, D P , and Yoshihara, H , "Oscillating Supercritical Airfoils in the Transonic Regime with Viscous Interaction " AGARD Conference Proceedings, Boundary Layer Effects on Unsteady Airloads, Aix-en-Province, France, Sept 1980

28 Rizzetta, D P , "Procedures for the Computation of Unsteady Transonic Flows Including Viscous Effects " NASA CR-166249, 1982

29 Goorjian, P M , and Van Buskirk, R , "Second Order Accurate Supersonic Differencing for the Small-Disturbance Potential Equations Applied to Transonic Flows " AIAA Paper 84-0091, Reno, Nev , 1984

30 Ballhaus, W F , and Goorjian, P M , "Efficient Solution of Unsteady Transonic Flows about Airfoils " AGARD Specialists Meeting on Unsteady Airloads in Separated and Transonic Flow, Lisbon, Portugal, AGARD Conference Proceedings No 226, Paper No 14, Apr 1977

31 Chow, L C , and Goorjian, P M , "Implicit Unsteady Transonic Airfoil Calculations at Supersonic Freestreams " AIAA Paper 82-0934, St Louis, Mo , 1982

32 Goorjian, P M , Meagher, M E , and Van Buskirk, R , "Monotone Implicit Algorithms for the Small-Disturbance and Full-Potential Equations Applied to Transonic Flows " AIAA Paper 83-0371, Reno, Nev , 1983

33 Kwak, D , "Nonreflecting Far-Field Boundary Conditions for Unsteady Transonic Flow Computations " AIAA Paper 80-1393, 1980

34 Guruswamy, P , and Goorjian, P M , "Effects of Viscosity on Transonic Aerodynamics and Aeroelastic Characteristics of Oscillating Airfoils " AIAA/ASCE/ASME/AHS Structures, Structural Dynamics, and Materials Conference, Lake Tahoe, Nev , May 1983

35 Guruswamy, P , and Goorjian, P M , "Development and Applications of XTRAN3S-AMES " Computational Fluid Dynamics User's Workshop, The University of Space Institute, Tullahoma, Tenn , Mar 1984

36 Davis, S , and Malcolm, G , "Experiments in Unsteady Transonic Flow " AIAA Paper 79-0769, 1979

37 Lambourne, N , "Compendium of Unsteady Aerodynamic Measurements " AGARD Report No 702, Aug 1982

38 Bucciantini, G , Oggiano, M S , and Onorato, M , "Supercritical Airfoil MBB-A3 Surface Pressure Distributions, Wake and Boundary Condition Measurements " Experimental Data Base for Computer Program Assessment, AGARD-AR-138, May 1979

39 Borland, C J , Rizzetta, D P , and Yoshihara, H , "Numerical Solution of Three Dimensional Unsteady Transonic Flow over Swept Wings " AIAA Paper 80-1369, Snowmass, Colo , 1980

40 Borland, C J , and Rizzetta, D P , "Nonlinear Transonic Flutter Analysis " AIAA Paper 81-0608-CP, Atlanta, Ga , 1981

41 Rizzetta, D P , and Borland, C J , "Numerical Solution of Three-Dimensional Unsteady Transonic Flow over Wings, Including Inviscid/Viscous Interaction " AIAA Paper 82-0352, 1982

42 Goorjian, P M , and Guruswamy, P , "Unsteady Transonics " Transonic Unsteady Aerodynamics and Aeroelasticity Workshop, NASA Langley Research Center, 1983

43 Guruswamy, P , and Goorjian, P M , "An Efficient Coordinate Transformation Technique for Unsteady Transonic Aerodynamic Analysis of Low Aspect Ratio Wings " AIAA Paper 84-0872-CP, Palm Springs, Calif , 1984

44 Marstiller, J W , Guruswamy, P , Yang, T Y , and Goorjian, P M , "Effects of Viscosity and Modes on Transonic Flutter Boundaries of Wings " AIAA Paper 84-0870-CP, Palm Springs, Calif , May 1984

45 Ballhaus, W F , Bailey, F R , and Frick, J , "Improved Computational Treatment of Transonic Flow about Swept Wings " Advances in Engineering Sciences, Vol 4, Nov 1976, pp 1311-1320

46 Fung, Y C , Theory of Aeroelasticity Dover Publications, Inc , New York, 1969

47 Lessing, H C , Troutman, J L , and Menees, G P , "Experimental Determination of the Pressure Distribution on a Rectangular Wing Oscillating in First Bending Mode for Mach Numbers from 0 24 to 1 30 " NASA TN D-344, 1960

48 Doggett, R V , Rainey, A G , and Morgan, H G , "An Experimental Investigation of Aerodynamic Effects of Airfoil Thickness on Transonic Flutter Characteristics " NASA TM X-79, 1959

49 Morita, T , Nakai, E , and Kikuchi, T , "An Experimental Investigation on the Transonic Flutter Characteristics of the Cantilever Swept-Back Wing with Aerofoil Section, and Comparison with the Thin Cantilever Swept Back Wing " National Aerospace Laboratory TR 361, Japan, 1974 (Also RAE Library Translation 1838, 1974 )

50 Tijdeman, J et al , "Transonic Wind Tunnel Tests on an Oscillating Wing with External Stores Pt II The Clean Wing " AFFDL-TR-78-194, Air Force Flight Dynamics Laboratory, Wright-Patterson AFB, Ohio, Mar 1979

51 Bisplinghoff, R L , Ashley, H , and Halfman, R L , Aeroelasticity Addison-Wesley Publishing Company, Menlo Park, Calif , 1957

52 Bland, S R , "AGARD Three Dimensional Aeroelastic Configurations." AGARD-AR-167, Mar 1982

ACKNOWLEDGMENT

We would like to thank Greg Kimberley (Informatics General Corp ) for the time-history plots of the two-dimensional calculations

Table 1 Comparisons of flutter speed and corresponding reduced frequency between LTRAN3 and experiment

| CASE | MACH NO | THICKNESS RATIO % | DENSITY RATIO $m/\pi\rho b^2$ | REDUCED FREQUENCY $\omega c/U$ LTRAN3 | REDUCED FREQUENCY $\omega c/U$ EXPT | FLUTTER SPEED $U/b\omega_\alpha$ LTRAN3 | FLUTTER SPEED $U/b\omega_\alpha$ EXPT |
|---|---|---|---|---|---|---|---|
| 1 | 0 715 | 6 | 36 72 | 0 250 | 0 232 | 4 30 | 3 83 |
| 2 | 0 851 | 6 | 58 72 | 0 120 | 0 162 | 5 60 | 4 55 |
| 3 | 0 913 | 6 | 74 65 | 0 045 | 0 122 | 8 80 | 4 94 |
| 4 | 0 904 | 4 | 75 17 | 0 085 | 0 138 | 6 60 | 3 70 |

Table 2 Flutter speeds for various modal combinations swept wing, M = 0 85

| MODES | INVISCID | WEDGE | LAG ENTRAINMENT |
|---|---|---|---|
| FIRST BENDING FIRST TORSION | 2 1237 | 2 8507 | 2 2066 |
| FIRST AND SECOND BENDING FIRST TORSION | 2 1240 | 2 8504 | 2 2057 |
| FIRST BENDING FIRST AND SECOND TORSION | 2 0666 | 2 9511 | 2 1856 |
| FIRST AND SECOND BENDING FIRST AND SECOND TORSION | 2 0670 | 2 9502 | 2 1850 |

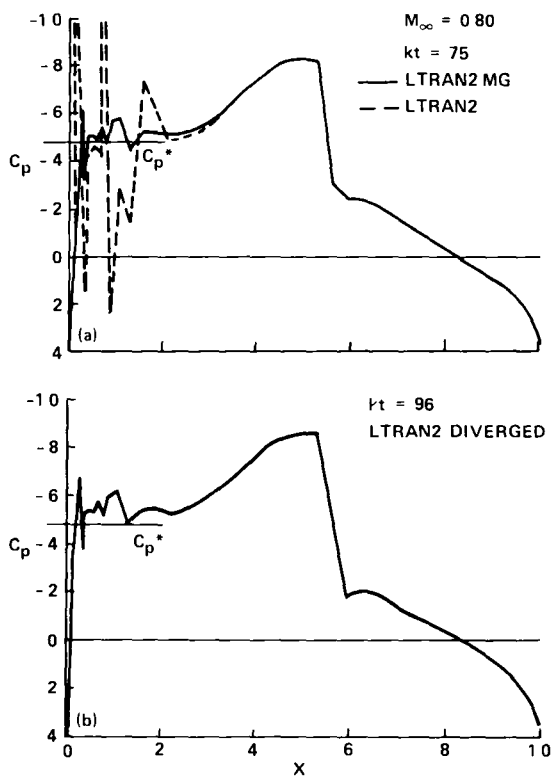


Fig 1 Comparison of algorithms using the monotone Godunov switch LTRAN2-MG and nonmonotone switch LTRAN2, plots of upper-surface pressure coefficients of a NACA 64A010 airfoil (experimental model ordinates) in pitching motion $M_\infty$ = 0 80

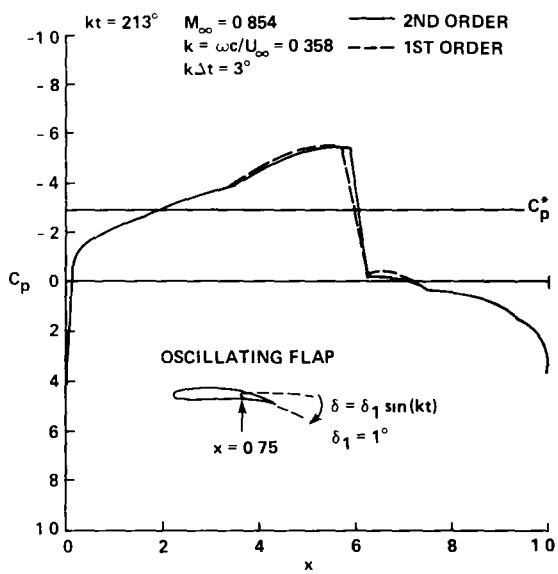


Fig 2 Comparison of first- and second-order methods for unsteady flow about a NACA 64A006 airfoil with oscillating trailing-edge flap, type-B shock-wave motion, instantaneous pressure-coefficient plots for upper surface kt = 213°

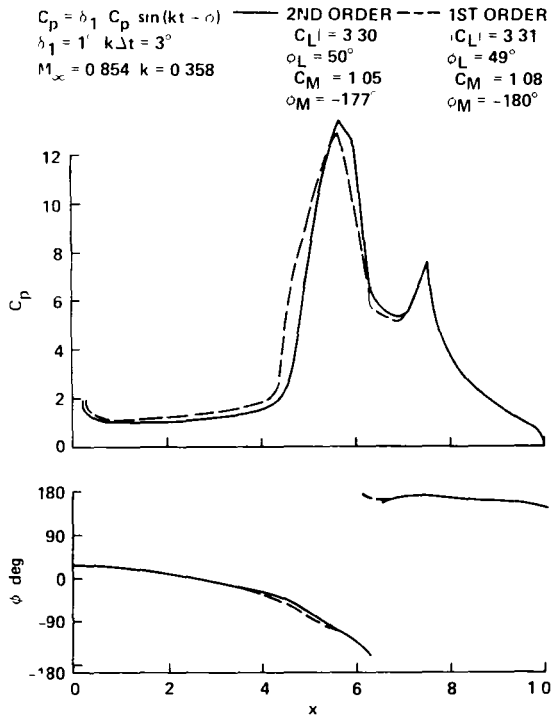


Fig 3 Unsteady upper-surface pressure-coefficient plots (amplitude and phase) of the first harmonic component for the case in Fig 2

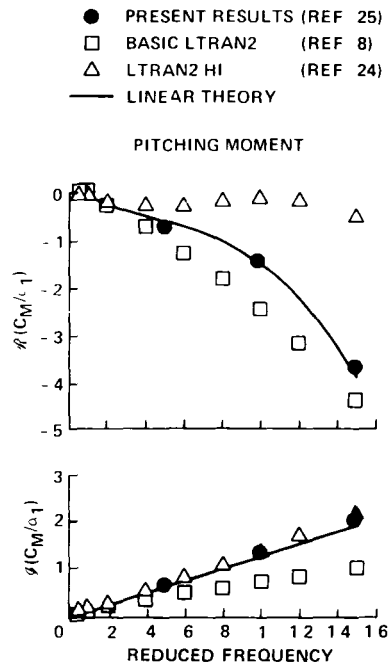


Fig 4 Real and imaginary components of pitching-moment coefficients for an airfoil oscillating in pitch $M_\infty = 0.7$, $\alpha = \alpha_i \sin \omega t$

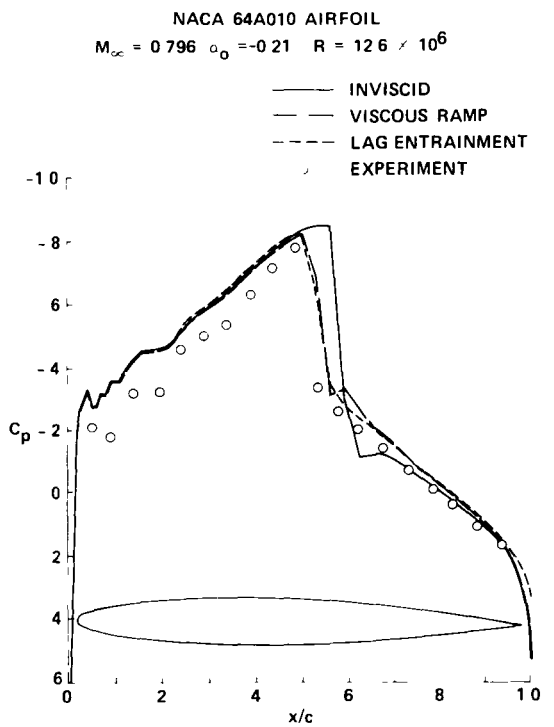


Fig 5 Comparison of lower-surface steady-pressure distributions, theories and experiment NACA 64A010 airfoil, M = 0.796

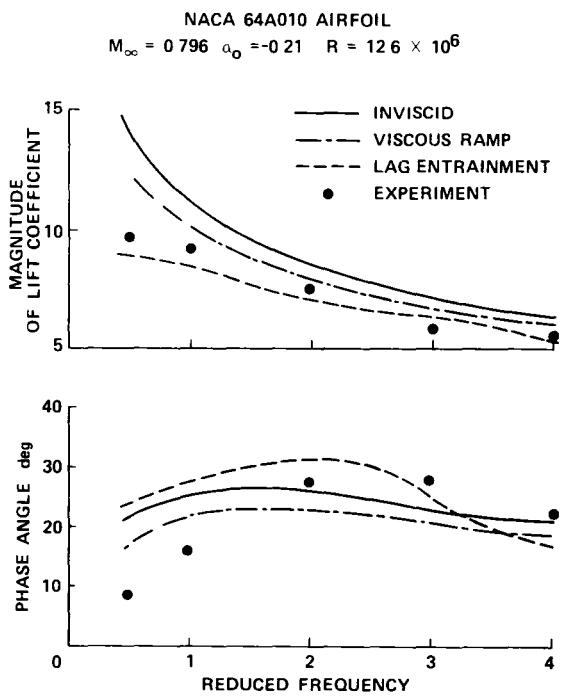


Fig 6 Comparison of plots of lift coefficient versus reduced frequency, theories and experiment

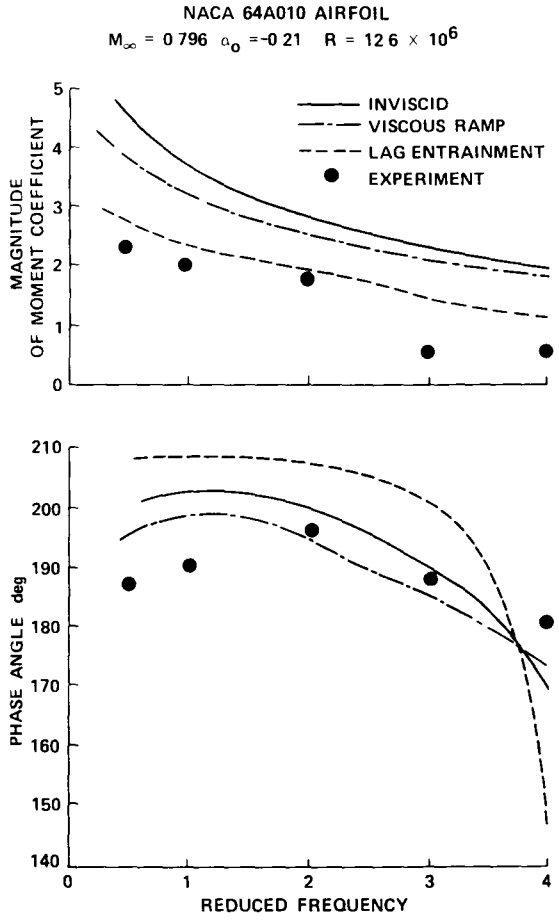


Fig 7 Comparison of plots of moment coefficient about leading edge versus reduced frequency, theories and experiment

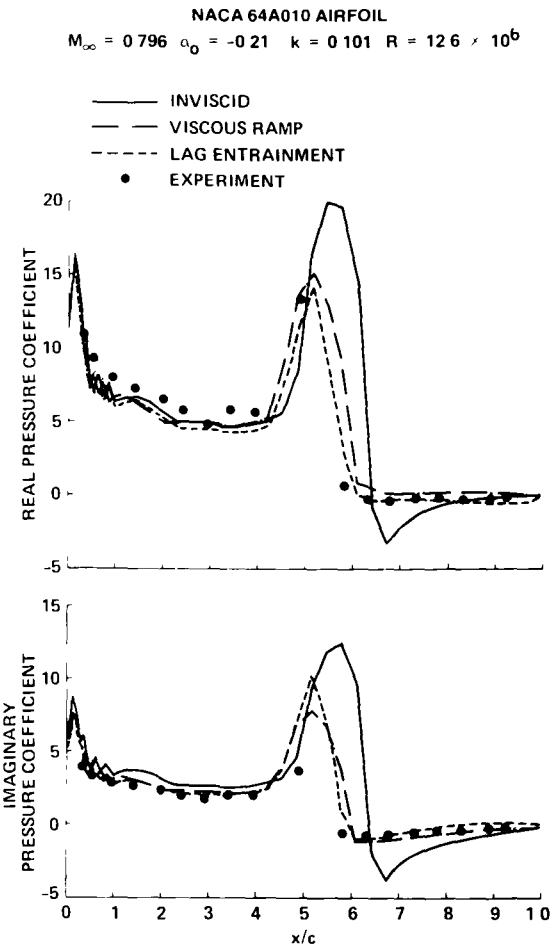


Fig 8 Real and imaginary parts of first Fourier component of unsteady lower-surface pressure coefficients k = 0 101

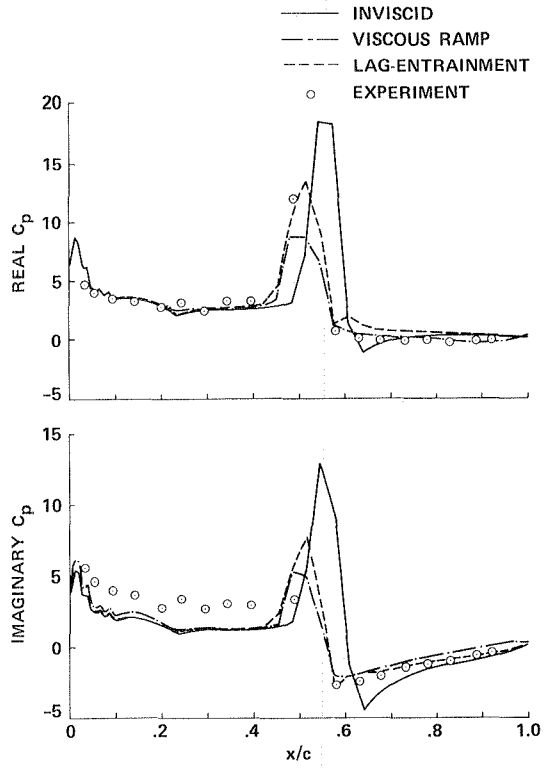


Fig. 9. Real and imaginary parts of first Fourier component of unsteady lower-surface pressure coefficients: k = 0.404.

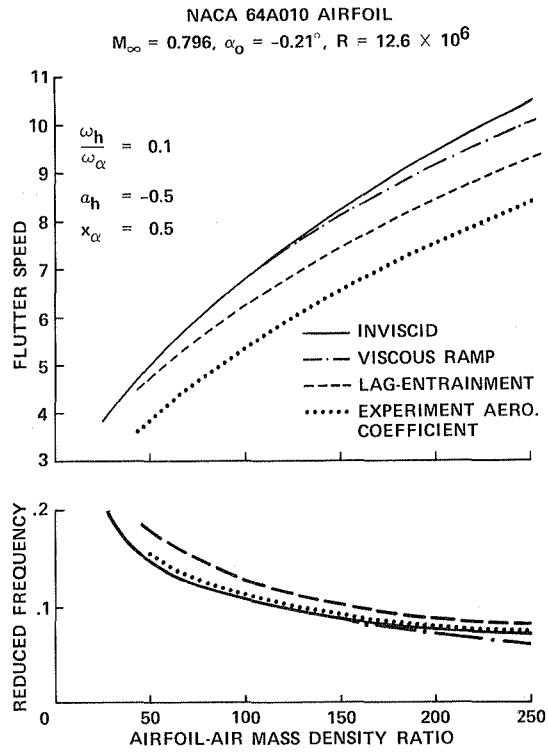


Fig. 10. Comparison of flutter speeds, theories and experiment.

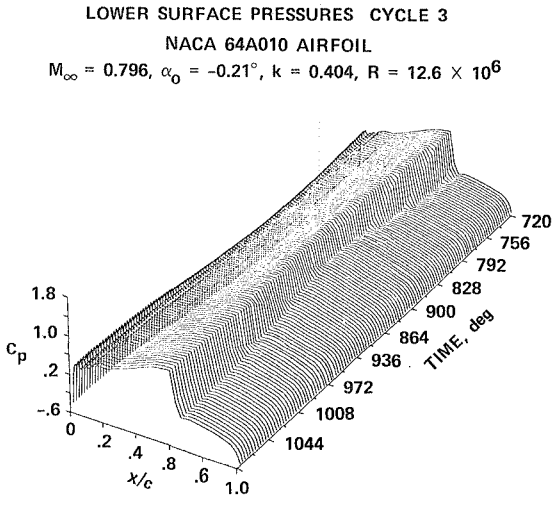


Fig. 11. Time-history of lower-surface pressure coefficients for third cycle of motion: NACA 64A010 airfoil, k = 0.404.

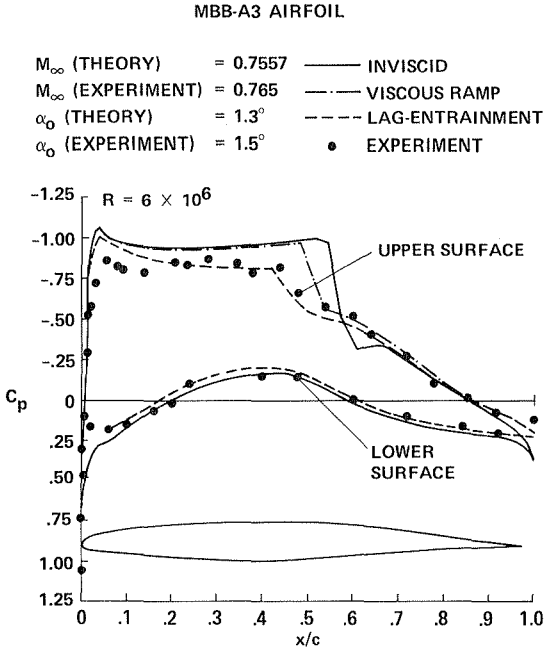


Fig. 12. Comparison of upper and lower surface steady-pressure distributions, theories and experiment.

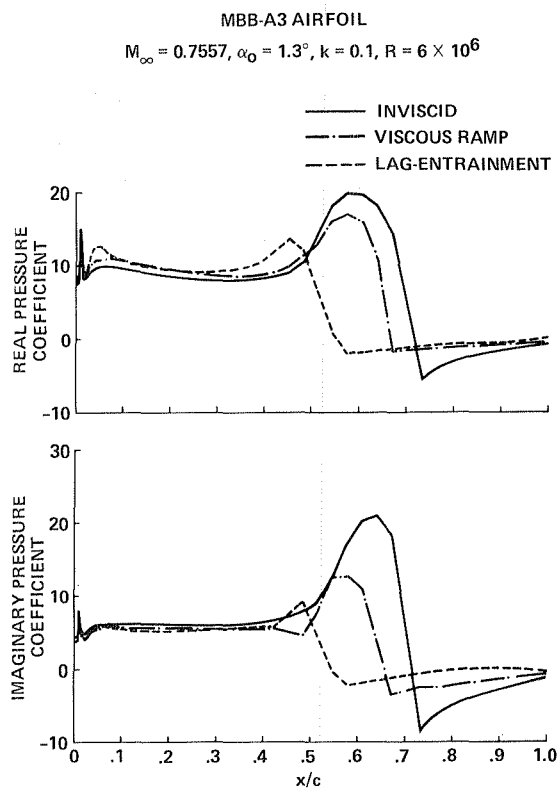


Fig. 13. Real and imaginary parts of first Fourier component of unsteady upper-surface pressure coefficients: k = 0.1.

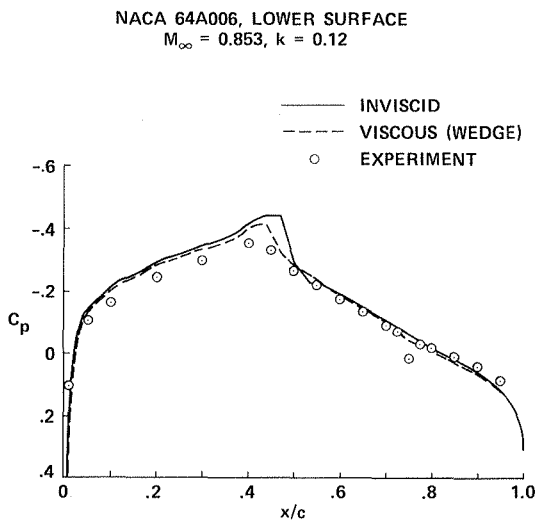


Fig. 14. Comparison of lower-surface steady-pressure distributions, theories and experiment: NACA 64A006, M = 0.853.

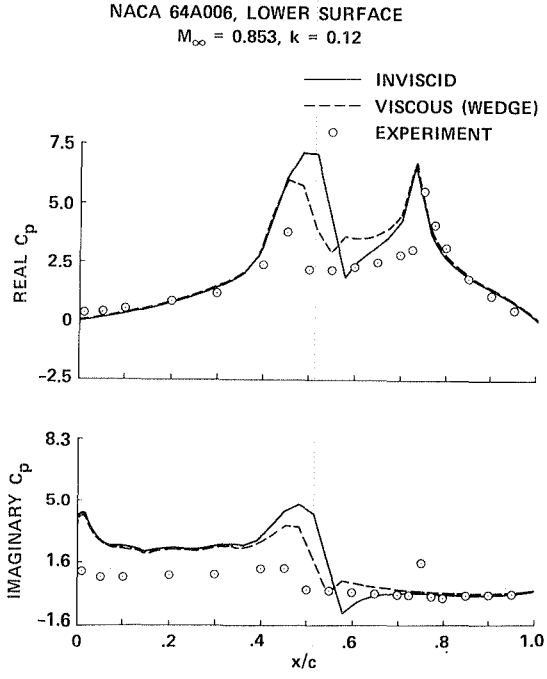


Fig. 15. Real and imaginary parts of first Fourier component of unsteady lower-surface pressure coefficients: k = 0.12.

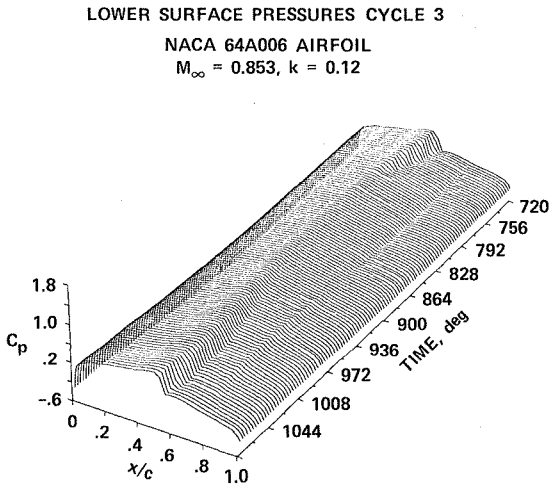


Fig. 16. Time-history of lower-surface pressure coefficients for third cycle of motion: NACA 64A006 airfoil, k = 0.12.

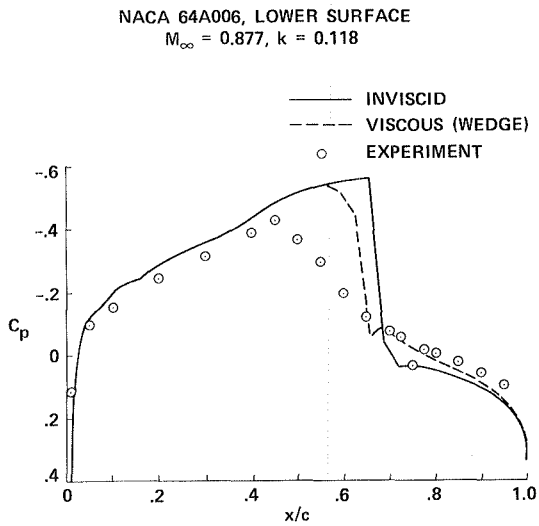


Fig. 17. Comparison of lower-surface steady pressure distributions, theories and experiment: NACA 64A006, M = 0.877.

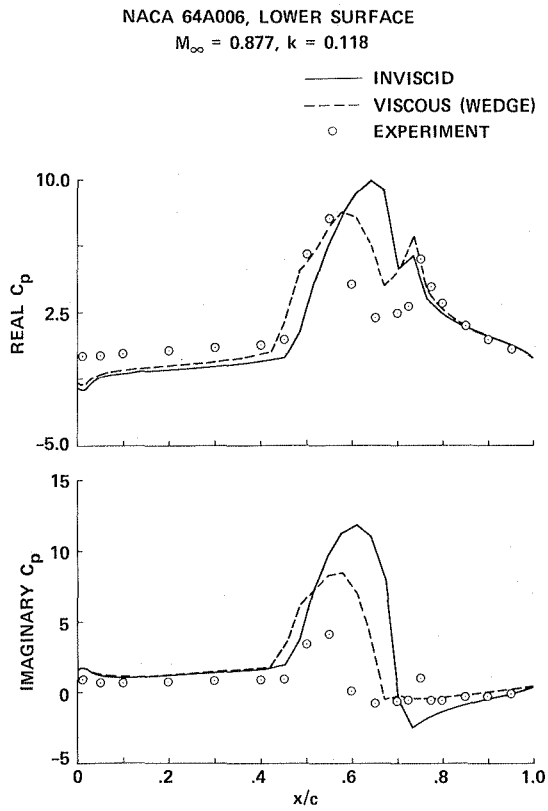


Fig. 18. Real and imaginary parts of first Fourier component of unsteady lower-surface pressure coefficients: NACA 64A006, k = 0.118.

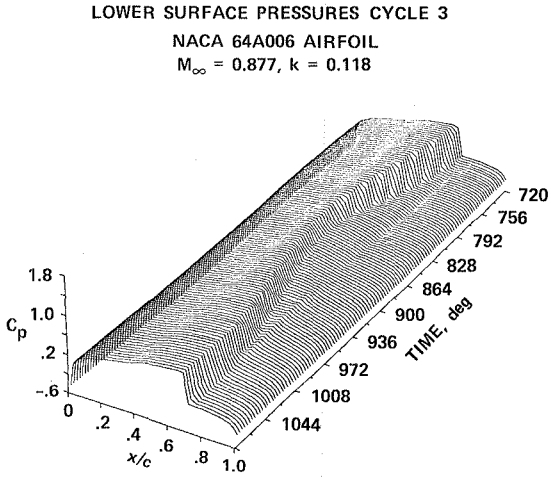


Fig. 19. Time-history of lower-surface pressure coefficients for the third cycle of motion: NACA 64A006 airfoil, k = 0.118, $M_\infty$ = 0.877.

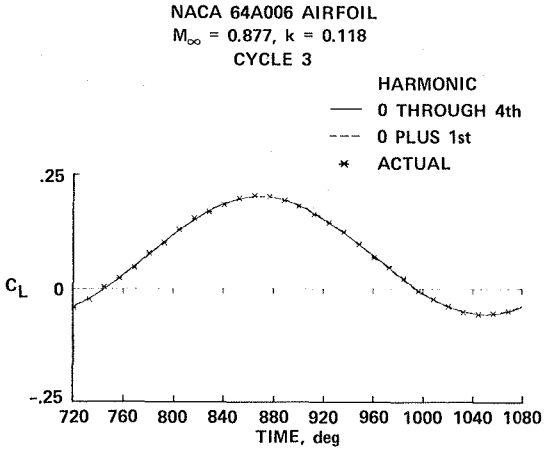


Fig. 20. Lift-coefficient variation during third cycle: NACA 64A006 airfoil, k = 0.118, $M_\infty$ = 0.877.

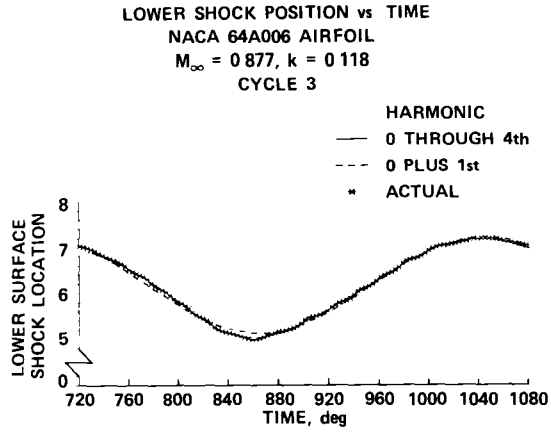


Fig 21 Lower-shock-position variation during third cycle NACA 64A006 airfoil, k = 0 118, $M_\infty$ = 0 877

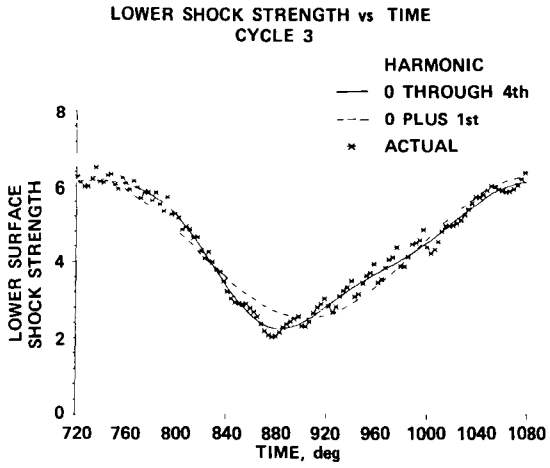


Fig 22 Lower-shock-strength variation during third cycle NACA 64A006 airfoil, k = 0 118, $M_\infty$ = 0 877

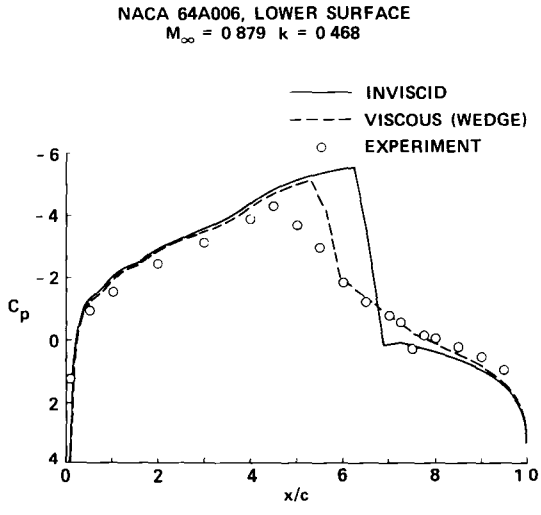


Fig 23 Comparison of lower-surface steady pressure distributions, theories and experiment NACA 64A006 airfoil, M = 0 879

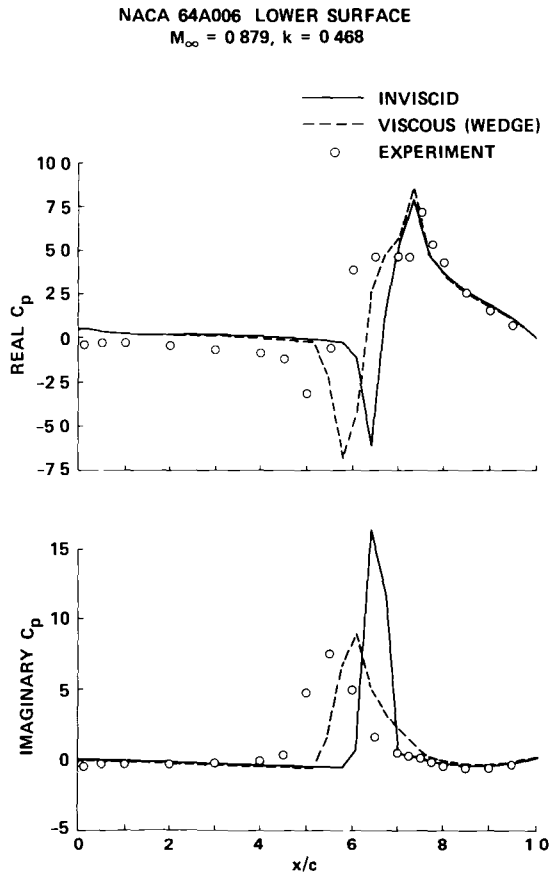


Fig 24 Real and imaginary parts of the first Fourier component of unsteady lower-surface pressure coefficients NACA 64A006, k = 0.468

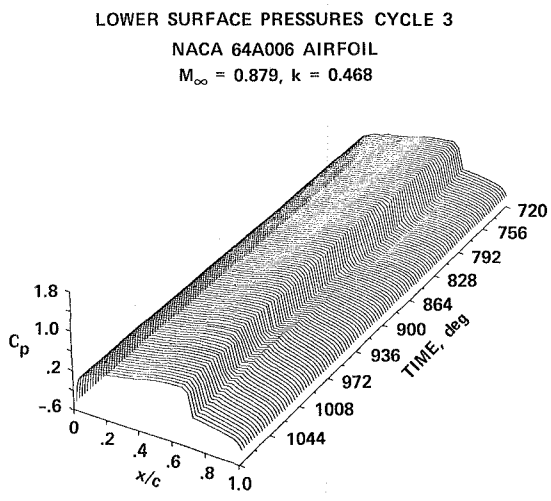


Fig. 25. Time-history of lower-surface pressure coefficients for the third cycle of motion: NACA 64A006 airfoil, k = 0.468, $M_\infty$ = 0.879.

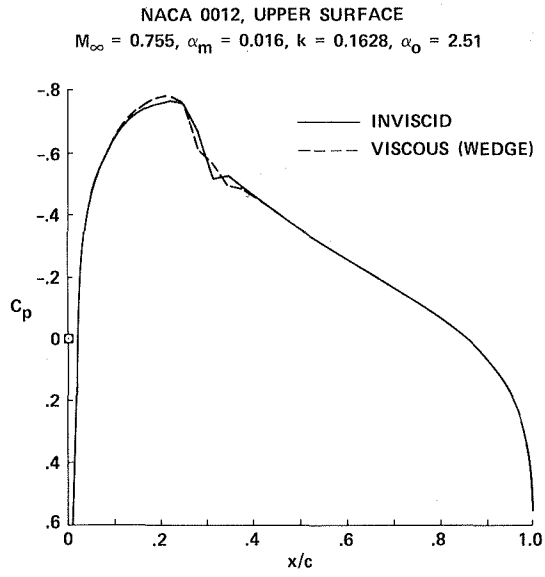


Fig. 26. Upper-surface steady pressure distributions: NACA 0012, M = 0.755.

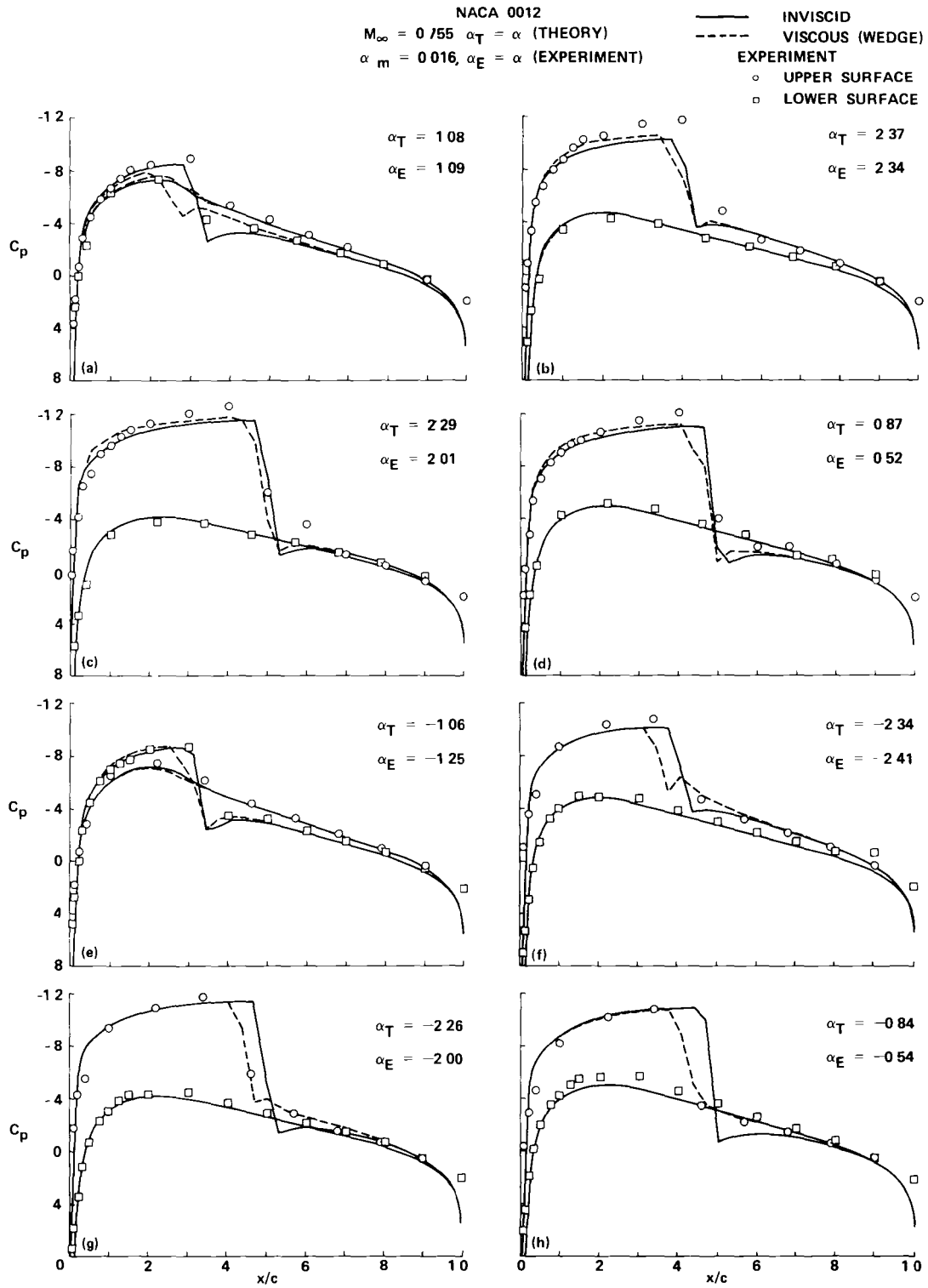


Fig 27 Comparisons of unsteady pressure coefficients during a cycle of motion, theories and experiment NACA 0012, $M_\infty$ = 0 755, k = 0 1628

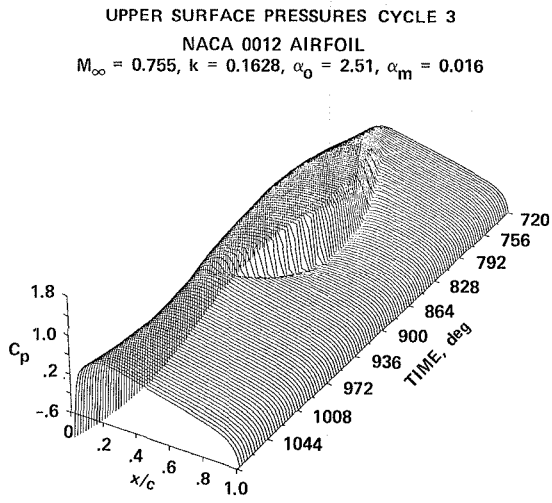


Fig. 28. Time-history of upper-surface pressure coefficients for the third cycle of motion: NACA 0012, $M_\infty$ = 0.755, k = 0.1628.

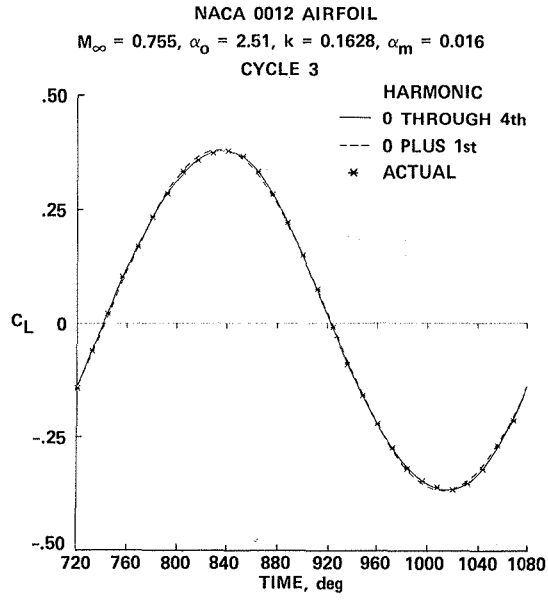


Fig. 29. Lift-coefficient variation during third cycle: NACA 0012, $M_\infty$ = 0.755, k = 0.1628.

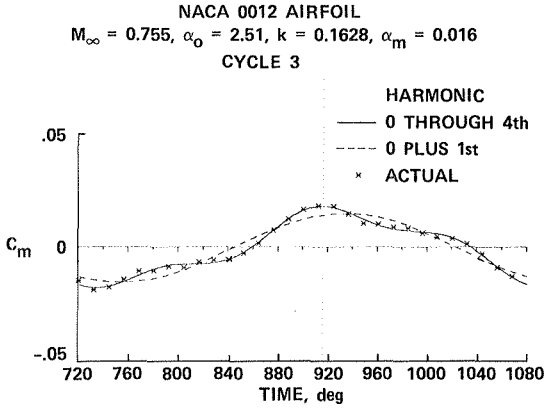


Fig. 30. Quarter-chord moment-coefficient variation during the third cycle: NACA 0012, $M_\infty$ = 0.755, k = 0.1628.

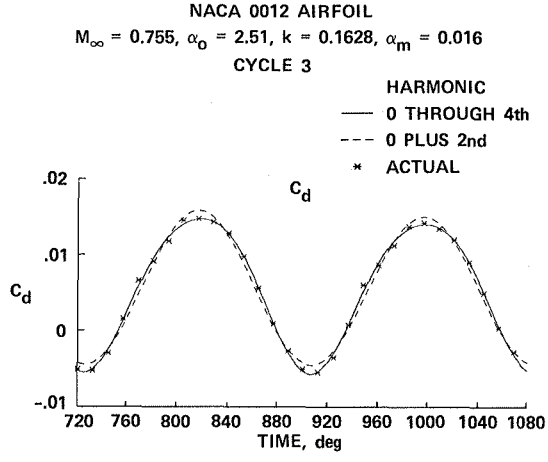


Fig. 31. Drag coefficient during third cycle: NACA 0012, $M_\infty$ = 0.755, k = 0.1628.

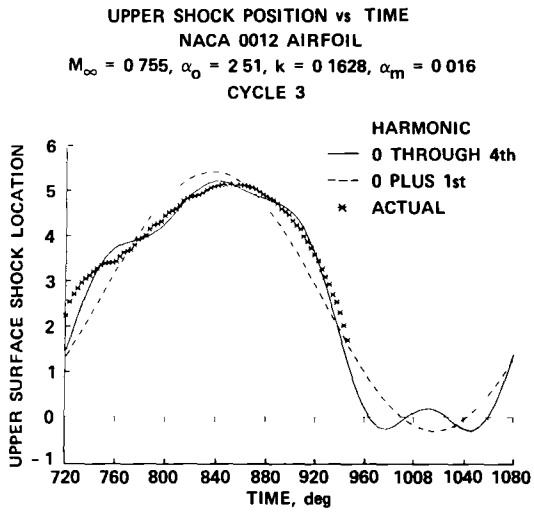


Fig 32 Upper-surface shock-position variation NACA 0012, $M_\infty$ = 0 755, k = 0 1628

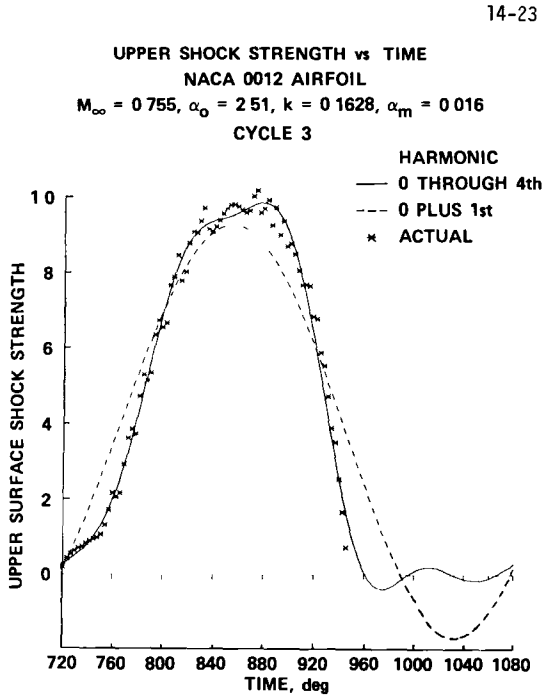


Fig 33 Upper-surface shock-strength variation NACA 0012, $M_\infty$ = 0 755, k = 0 1628

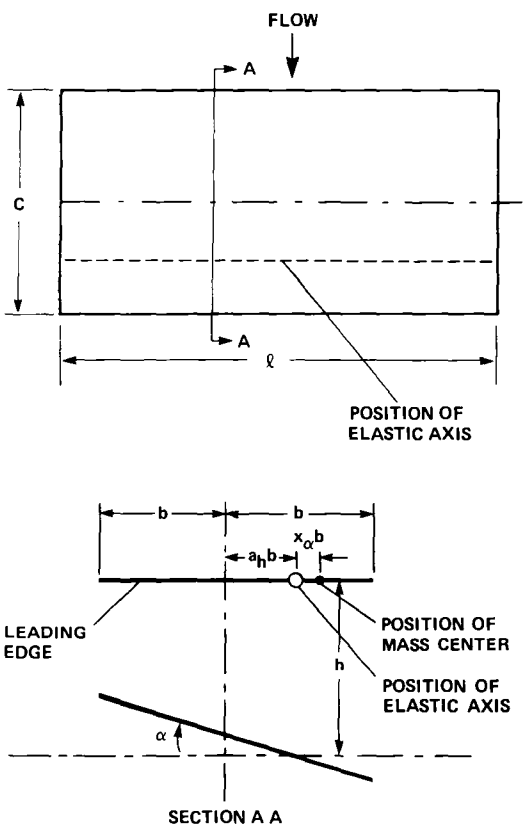


Fig 34 Definition of aeroelastic parameters for a cantilever wing

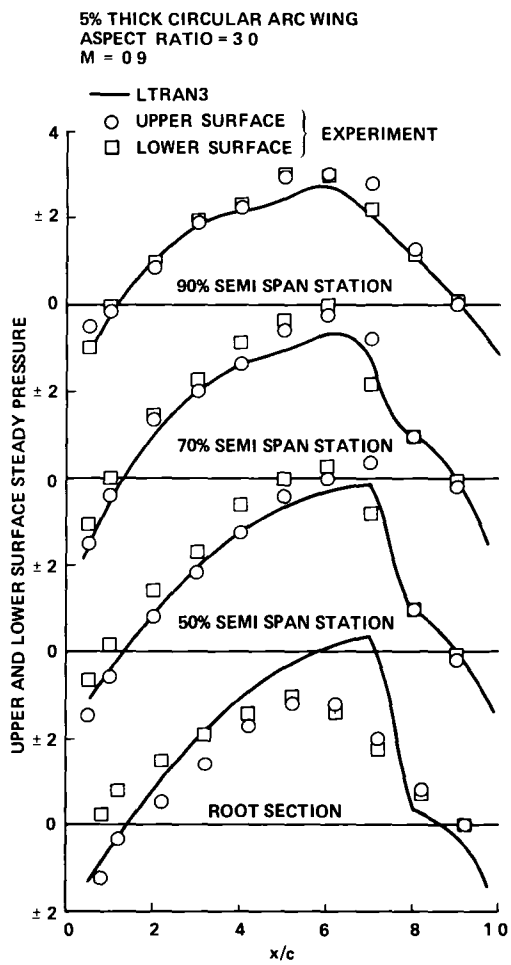


Fig 35 Comparison of steady pressure coefficients LTRAN3 and experiment

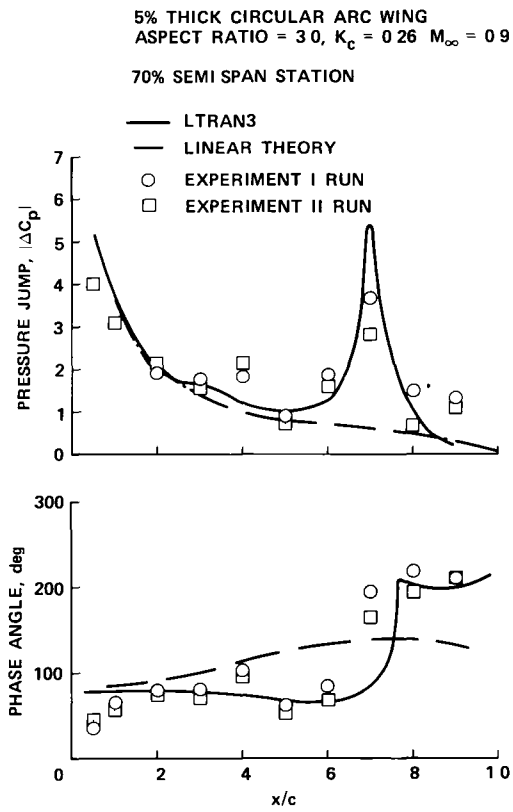


Fig 36 Comparison of magnitude and corresponding phase angle of pressure jumps among results obtained by LTRAN3 experiment and linear theory

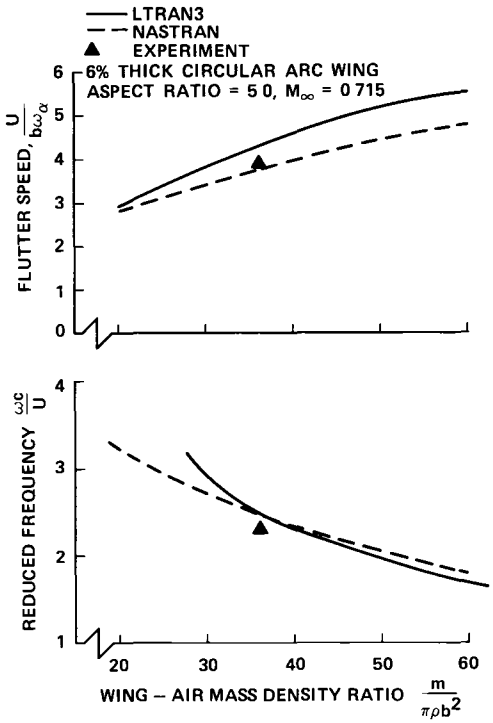


Fig 37 Comparison of flutter speed and corresponding reduced frequency results obtained by LTRAN3, experiment, and NASTRAN for case 1

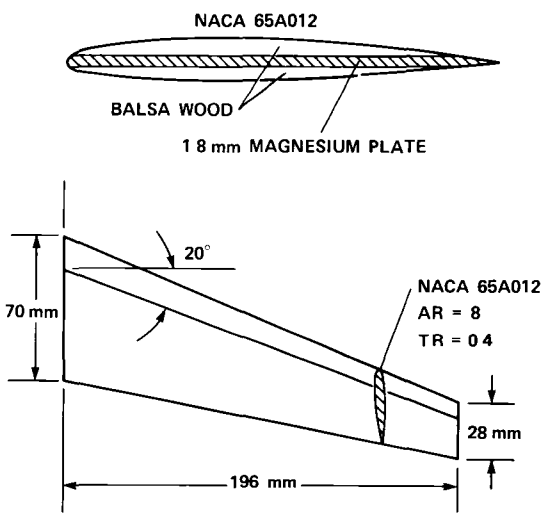


Fig 38 Code correlation model of Japanese transport wing

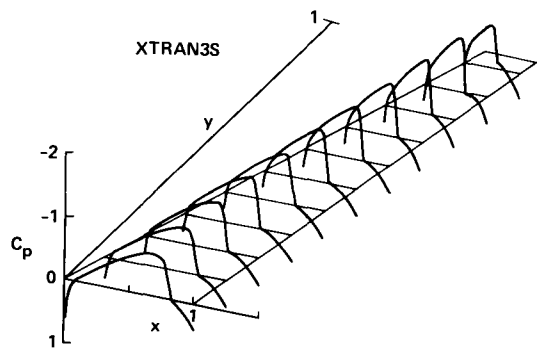


Fig 39. Steady-state initial conditions for Japanese transport wing $M_\infty$ = 0 85

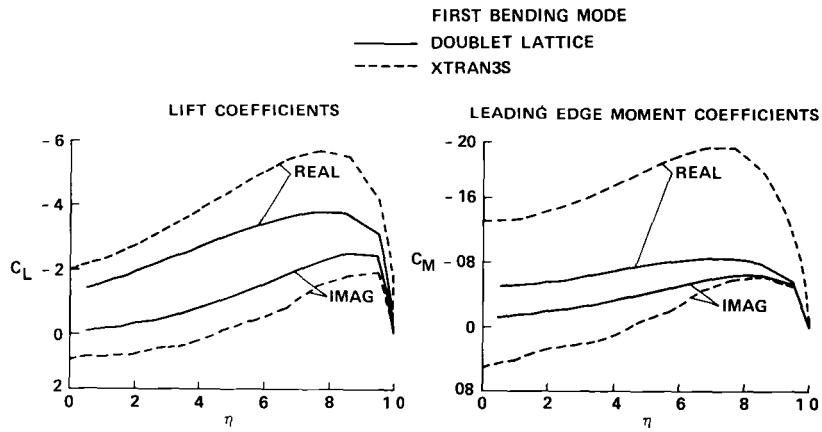


Fig 40 Modal aerodynamics for the Japanese transport wing $M_\infty$ = 0 85, k = 0 121

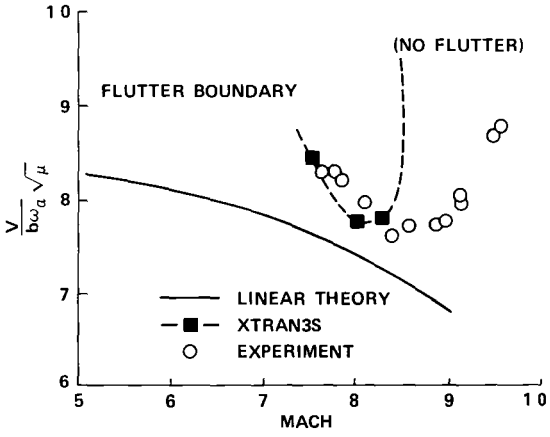


Fig 41 XTRAN3S flutter boundary for the Japanese transport wing

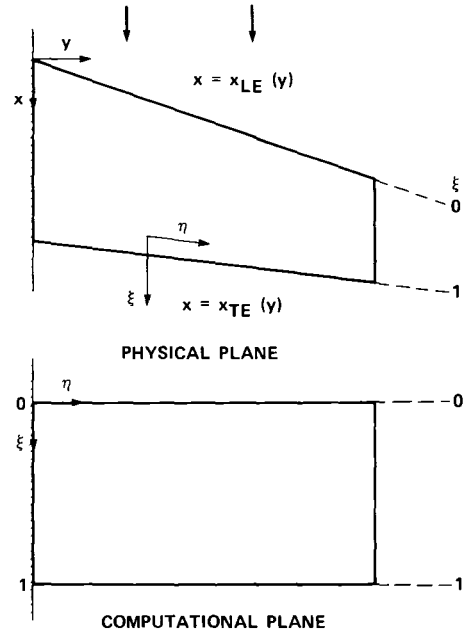


Fig. 42. Sheared coordinate system ξ,η,ζ used for swept and tapered wings

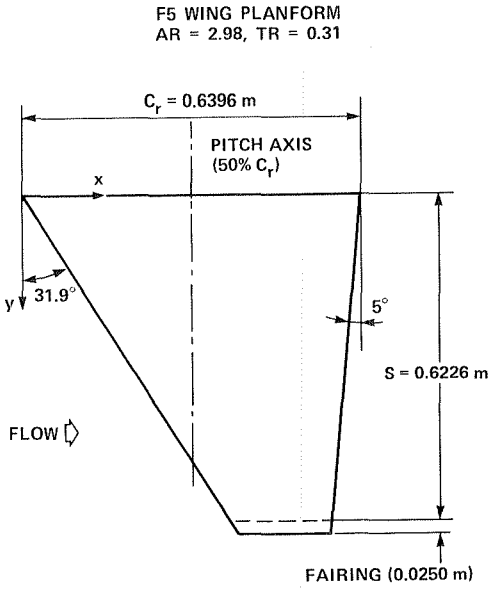


Fig. 43. Dimensions of the F-5 wing.

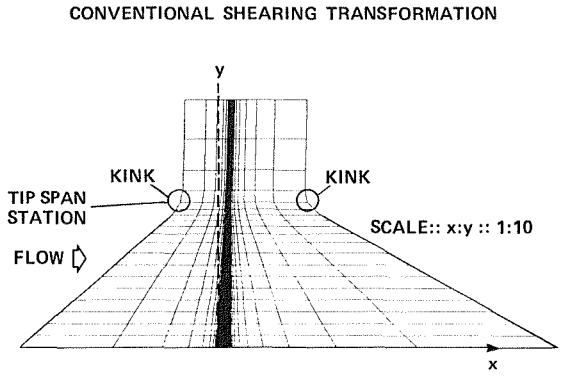


Fig. 44. Physical grid (64 × 20) in x-y plane from the conventional shearing transformation.

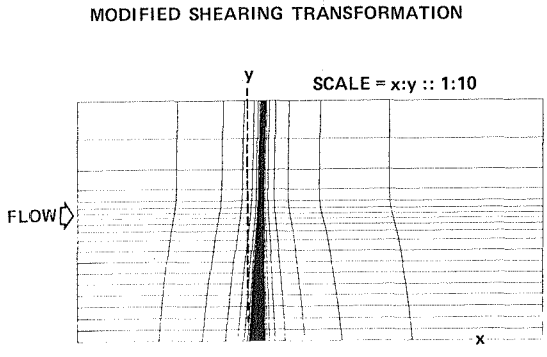


Fig. 45. Physical grid (64 × 20) in x-y plane by the modified shearing transformation.

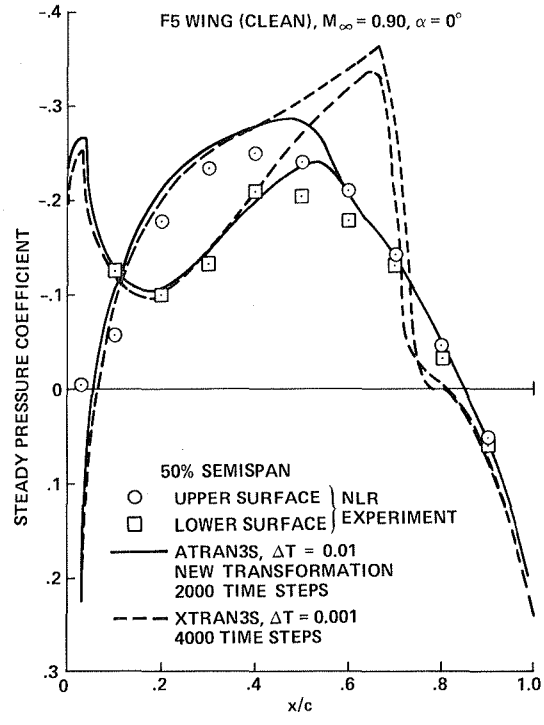


Fig. 46. Effect of transformation on steady pressures at M = 0.90.

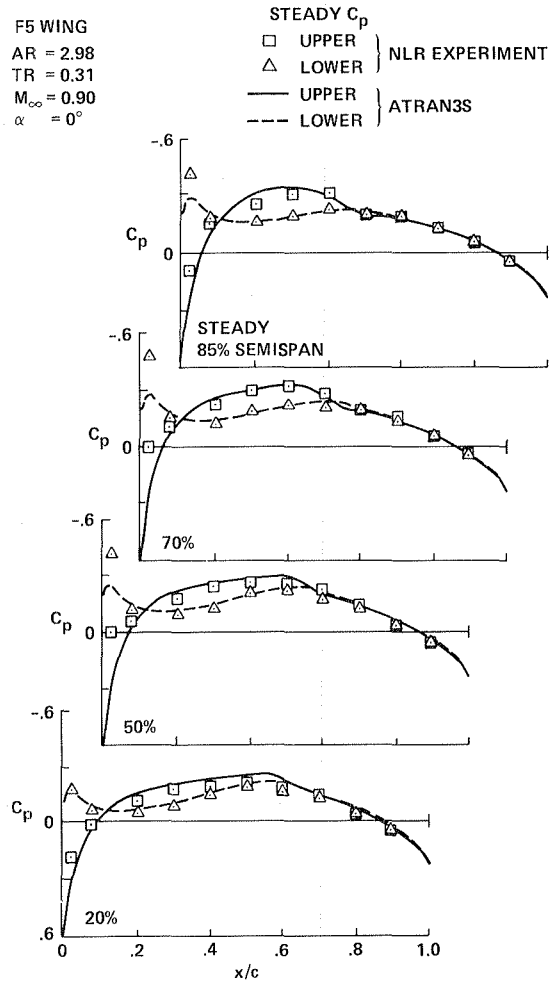


Fig. 47. Comparison of steady pressures, theory and experiment: M = 0.90.

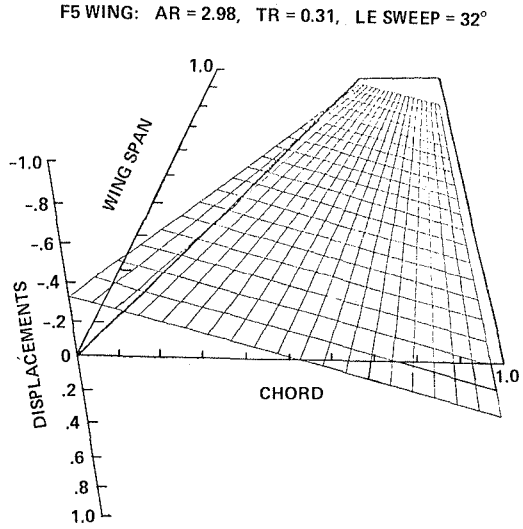


Fig. 48. Unsteady modal motion of the F-5 wing.

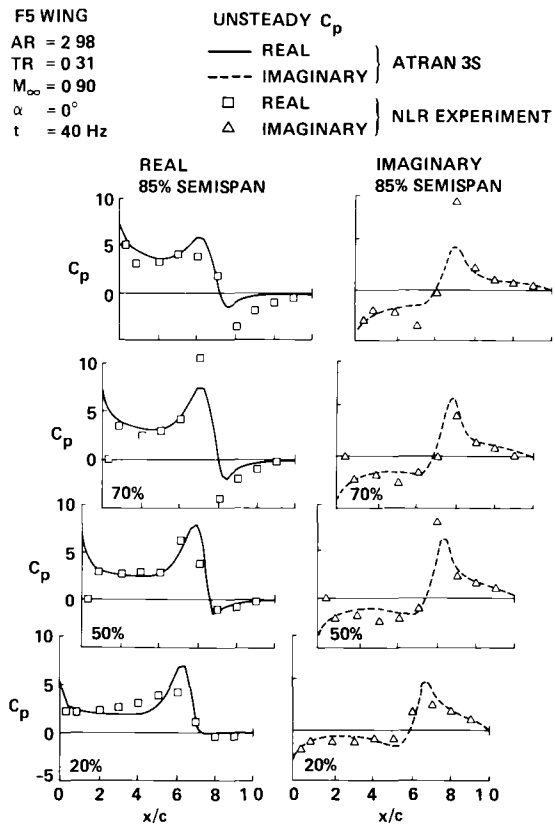


Fig 49 Comparison of unsteady pressures, theory and experiment M = 0 90

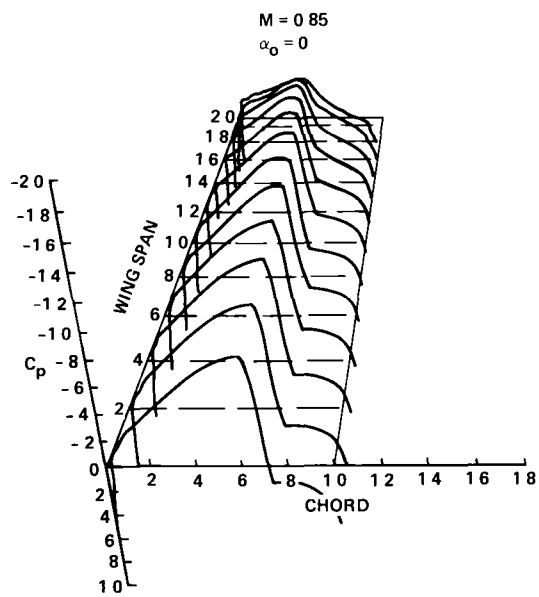


Fig 50 Rectangular wing steady pressure distributions M = 0 85

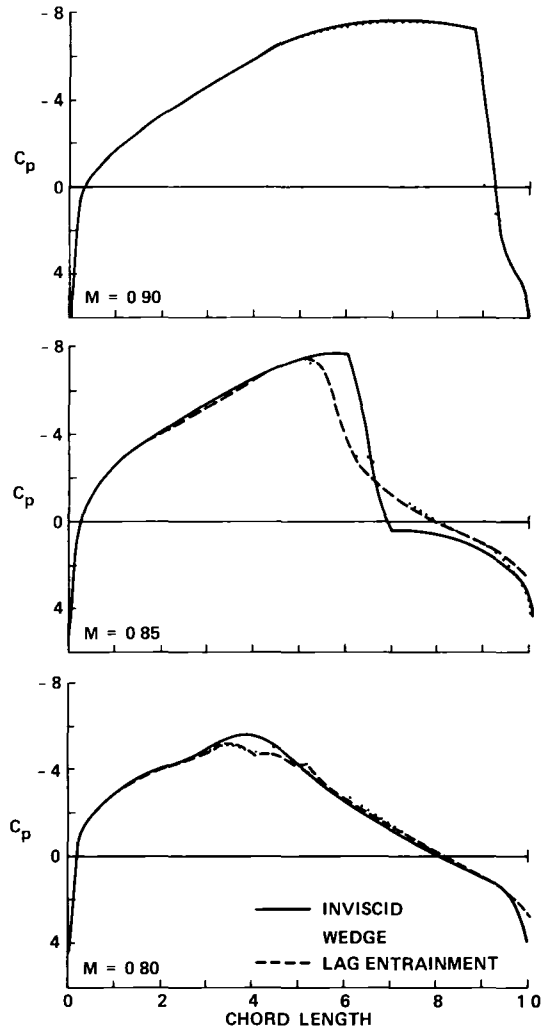


Fig 51 Rectangular wing steady pressure shown for three Mach numbers and the inviscid and viscous methods at 60% semispan station and $\alpha = 0$

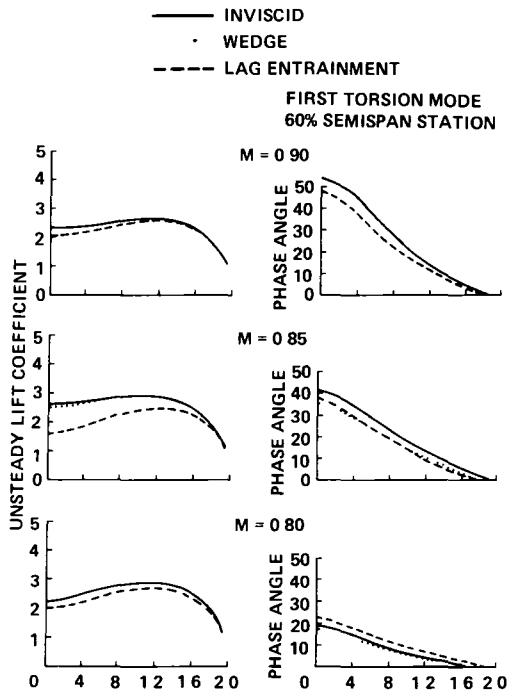


Fig 52 Magnitude of unsteady lift and corresponding phase angle versus span for the inviscid and viscous methods

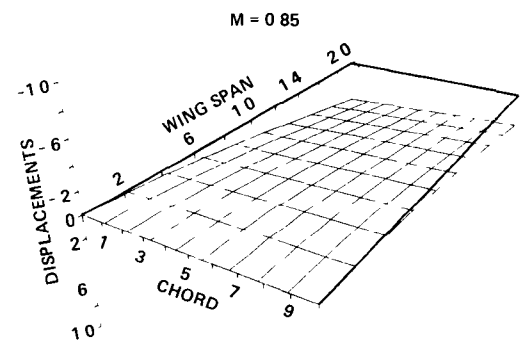


Fig 53 The shape of the rectangular wing at flutter is composed of the first bending and torsion modes

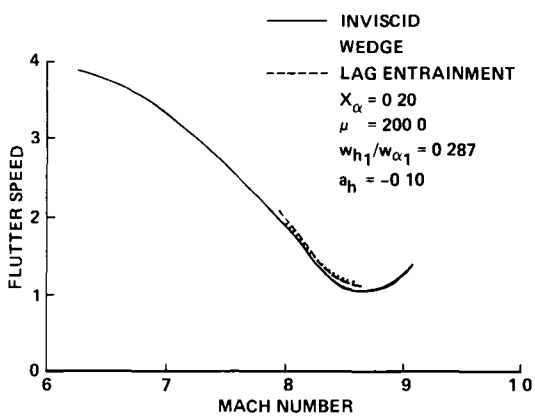


Fig 54 Effect of Mach number and viscosity on flutter speed of the rectangular wing

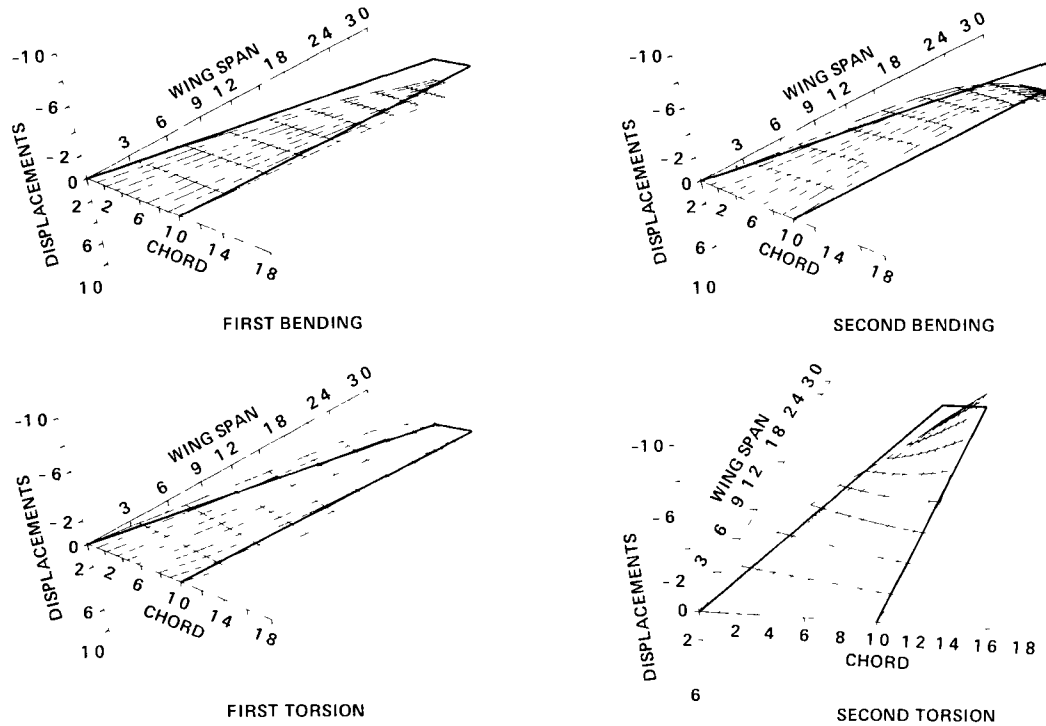


Fig 55 Swept-wing beam mode shapes

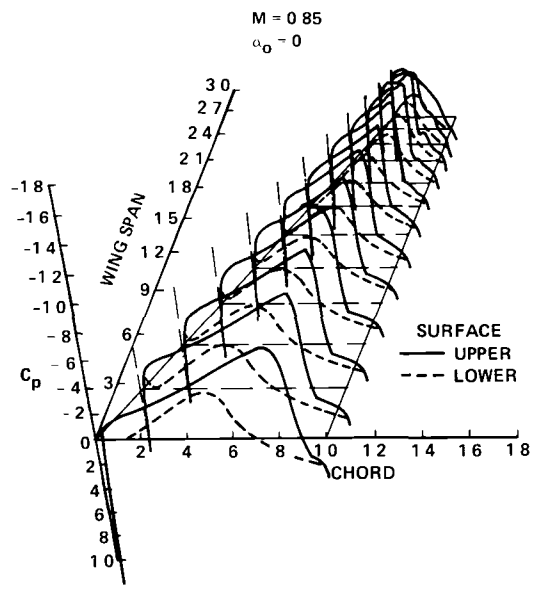


Fig 56 Swept-wing steady-pressure distributions

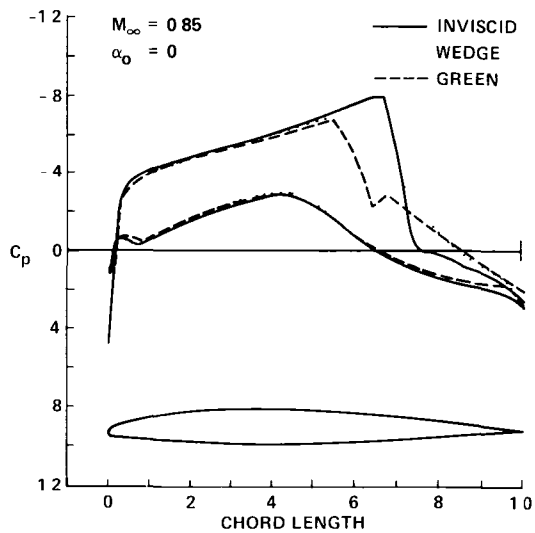


Fig 57 Swept-wing steady pressure for the inviscid and viscous methods 60% semispan, $\alpha$ = 0

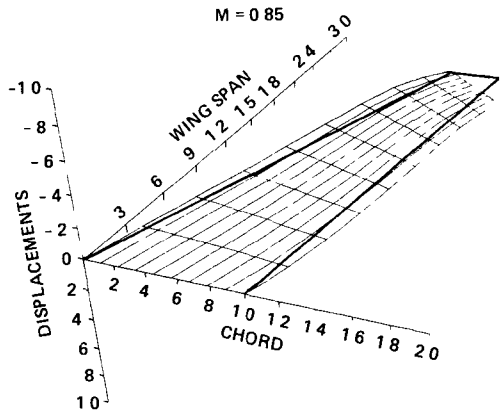


Fig 58 Shape of the swept wing at flutter is composed of the first bending and the first and second torsion modes

| 1 Report No | 2 Government Accession No | 3 Recipient's Catalog No |
|---|---|---|
| NASA TM-85986 | | |

| 4 Title and Subtitle | 5 Report Date |
|---|---|
| UNSTEADY TRANSONIC AERODYNAMIC AND AEROELASTIC CALCULATIONS ABOUT AIRFOILS AND WINGS | August 1984 |
| | 6 Performing Organization Code |
| 7 Author(s) Peter M. Goorjian (Ames Research Center) and Guru P. Guruswamy (Informatics General Corp., Palo Alto, CA) | 8 Performing Organization Report No A-9822 |
| 9 Performing Organization Name and Address NASA Ames Research Center Moffett Field, CA 94035 | 10 Work Unit No T-6458 |
| | 11 Contract or Grant No |
| 12 Sponsoring Agency Name and Address National Aeronautics and Space Administration Washington, DC 20546 | 13 Type of Report and Period Covered Technical Memorandum |
| | 14 Sponsoring Agency Code 505-31-01 |

15 Supplementary Notes

Point of Contact: Peter M. Goorjian, Ames Research Center, MS 202A-14, Moffett Field, CA 94035. (415) 965-5547 or FTS 448-5547.

16 Abstract

The development and application of transonic small-disturbance codes at NASA Ames Research Center for computing two-dimensional flows, using the code ATRAN2, and for computing three-dimensional flows, using the code ATRAN3S, are described. Calculated and experimental results are compared for unsteady flows about airfoils and wings, including several of the cases from the AGARD Standard Aeroelastic Configurations. In two dimensions, the results include AGARD priority cases for the NACA 64A006, NACA 64A010, NACA 0012, and MBB-A3 airfoils. In three dimensions, the results include flows about the F-5 wing, a typical transport wing, and the AGARD rectangular wing. Viscous corrections are included in some calculations, including those for the AGARD rectangular wing. For several cases, the aerodynamic and aeroelastic calculations are compared with experimental results.

| 17 Key Words (Suggested by Author(s)) | 18 Distribution Statement |
|---|---|
| Unsteady transonic<br>Aerodynamic calculations | Unlimited<br><br>Subject Category - 02 |

| 19 Security Classif (of this report) | 20 Security Classif (of this page) | 21 No of Pages | 22 Price* |
|---|---|---|---|
| Unclassified | Unclassified | 34 | A02 |

*For sale by the National Technical Information Service Springfield Virginia 22161

**End of Document**